

## RELICS: THE REIONIZATION LENSING CLUSTER SURVEY AND THE BRIGHTEST HIGH-Z GALAXIES

BRETT SALMON<sup>1,†</sup>, DAN COE<sup>1</sup>, LARRY BRADLEY<sup>1</sup>, RYCHARD BOUWENS<sup>2</sup>, MARUSA BRADAČ<sup>3</sup>, KUANG-HAN HUANG<sup>3</sup>, PASCAL OESCH<sup>4</sup>, DANIEL STARK<sup>5</sup>, KEREN SHARON<sup>6</sup>, MICHELE TRENTI<sup>7</sup>, ROBERTO J. AVILA<sup>1</sup>, SARA OGAZ<sup>1</sup>, FELIPE ANDRADE-SANTOS<sup>8</sup>, DANIELA CARRASCO<sup>7</sup>, CATHERINE CERNY<sup>6</sup>, WILLIAM DAWSON<sup>9</sup>, BRENDA L. FRYE<sup>5</sup>, AUSTIN HOAG<sup>3</sup>, TRACI LIN JOHNSON<sup>6</sup>, CHRISTINE JONES<sup>8</sup>, DANIEL LAM<sup>2</sup>, LORENZO LOVISARI<sup>8</sup>, RAMESH MAINALI<sup>5</sup>, MATT PAST<sup>6</sup>, RACHEL PATERNO-MAHLER<sup>6</sup>, AVERY PETERSON<sup>6</sup>, ADAM G. RIESS<sup>10,1</sup>, STEVEN A. RODNEY<sup>11</sup>, RUSSEL E. RYAN<sup>1</sup>, IRENE SENDRA-SERVER<sup>12</sup>, LOUIS-GREGORY STROLGER<sup>1</sup>, KEIICHI UMETSU<sup>13</sup>, BENEDETTA VULCANI<sup>7</sup>, ADI ZITRIN<sup>14</sup>

<sup>1</sup>Space Telescope Science Institute, Baltimore, MD, USA,

<sup>2</sup>Leiden Observatory, Leiden University, NL-2300 RA Leiden, The Netherlands,

<sup>3</sup>Department of Physics, University of California, Davis, CA 95616, USA,

<sup>4</sup>Geneva Observatory, University of Geneva, Ch. des Maillettes 51, 1290 Versoix, Switzerland,

<sup>5</sup>Department of Astronomy, Steward Observatory, University of Arizona, 933 North Cherry Avenue, Rm N204, Tucson, AZ, 85721, USA,

<sup>6</sup>Department of Astronomy, University of Michigan, 1085 South University Ave, Ann Arbor, MI 48109, USA,

<sup>7</sup>School of Physics, University of Melbourne, VIC 3010, Australia,

<sup>8</sup>Harvard-Smithsonian Center for Astrophysics, 60 Garden Street, Cambridge, MA 02138, USA,

<sup>9</sup>Lawrence Livermore National Laboratory, P.O. Box 808 L- 210, Livermore, CA, 94551, USA,

<sup>10</sup>Department of Physics and Astronomy, The Johns Hopkins University, Baltimore, MD 21218,

<sup>11</sup>Department of Physics and Astronomy, University of South Carolina, 712 Main St., Columbia, SC 29208, USA,

<sup>12</sup>Infrared Processing and Analysis Center, California Institute of Technology, MS 100-22, Pasadena, CA 91125

<sup>13</sup>Institute of Astronomy and Astrophysics, Academia Sinica, PO Box 23-141, Taipei 10617, Taiwan

<sup>14</sup>Physics Department, Ben-Gurion University of the Negev, P.O. Box 653, Beer-Sheva 84105, Israel

*Submitted to ApJ*

### ABSTRACT

Massive foreground galaxy clusters magnify and distort the light of objects behind them, permitting a view into both the extremely distant and intrinsically faint galaxy populations. We present here the  $z \sim 6 - 8$  candidate high-redshift galaxies from the Reionization Lensing Cluster Survey (RELICS), a *Hubble* and *Spitzer Space Telescope* survey of 41 massive galaxy clusters spanning an area of  $\approx 200$  arcmin<sup>2</sup>. These clusters were selected to be excellent lenses and we find similar high-redshift sample sizes and magnitude distributions as CLASH. We discover 321 candidate galaxies with photometric redshifts between  $z \sim 6$  to  $z \sim 8$ , including extremely bright objects with  $H$ -band magnitudes of  $m_{AB} \approx 23$  mag. As a sample, the observed (lensed) magnitudes of these galaxies are among the brightest known at  $z \geq 6$ , comparable to much wider, blank-field surveys. RELICS demonstrates the efficiency of using strong gravitational lenses to produce high-redshift samples in the epoch of reionization. These brightly observed galaxies are excellent targets for follow-up study with current and future observatories, including the James Webb Space Telescope.

*Keywords:* galaxies: high-redshift — galaxies: evolution — galaxies: clusters: general — galaxies: luminosity function, mass function — gravitational lensing: strong

### 1. INTRODUCTION

Images from modern extragalactic surveys are rich with red sources as we push deeper to reveal the faint, redshifted population of the very first galaxies. Our investment in this early epoch is for good reason; the first billion years of the universe ( $t_{\text{universe}} \approx 1$  Gyr at  $z = 5.5$ ) cover an era of rapid evolution both in the first stars and the first galaxies (for a complete review, see Stark 2016). Moreover, this period spans the time when the universe undergoes a phase transition from being primarily neutral to primarily ionized in a process called reionization. Understanding the properties and relative number of intrinsically faint and bright galaxies at this epoch directly affects our interpretation of how reionization occurred, given that the most likely culprits for reionization were intrinsically faint galaxies at  $z > 6$  (Madau et al. 1999; Yan et al. 2003; Bunker et al. 2004; Oesch et al. 2009; Kuhlen & Faucher-Giguère 2012; Finkelstein et al. 2012; McLure et al. 2013; Schmidt et al. 2014; Robertson et al.

2015; Atek et al. 2015a; Ishigaki et al. 2015; Bouwens et al. 2017b; Livermore et al. 2017).

There have been a variety of approaches to reach this distant galaxy population. While more costly, deep space-based, blank-field surveys such as the Cosmic Assembly Deep Extragalactic Legacy Survey (CANDELS; Grogin et al. 2011; Koekemoer et al. 2011) and the Hubble Ultra Deep Field (HUDF; Beckwith et al. 2006; Bouwens et al. 2011; Ellis et al. 2013; Koekemoer et al. 2013; Illingworth et al. 2013) as well as wide surveys such as the Brightest of Reionization Galaxies (BoRG; Trenti et al. 2011; Bradley et al. 2012) and UltraVista (Scoville et al. 2007; McCracken et al. 2012; Bowler et al. 2012, 2017) have produced exquisite datasets that comprise some of the largest and brightest samples of  $3 < z < 10$  galaxies. The recent ground-based  $z = 6 - 7$  samples from the GOLDRUSH (Harikane et al. 2017; Ono et al. 2017) and SILVERRUSH (Konno et al. 2017; Shibuya et al. 2017a,b; Ouchi et al. 2017) surveys have discovered thousands of high- $z$  galaxies and valuable insight into the behavior of Lyman- $\alpha$  1216 Å emission in the epoch

† bsalmon@stsci.edu

of reionization. These surveys continue to surprise us with results from the distant universe, including the inexplicably bright, most distant confirmed galaxy found to-date at  $z = 11.1$  ( $t_{\text{universe}} \approx 400$  Myr; Oesch et al. 2016).

Another approach is to take advantage of natural telescopes by observing strong gravitational lenses. Cluster lensing surveys such as the Cluster Lensing and Supernovae Survey with Hubble (CLASH; Zheng et al. 2012; Postman et al. 2012; Coe et al. 2013; Bradley et al. 2014; Bouwens et al. 2014) and the Hubble Frontier Fields (HFF; Coe et al. 2015; Atek et al. 2015b,a; Lotz et al. 2017; Ishigaki et al. 2017; Bouwens et al. 2017b) have produced most of the  $z \geq 8$  galaxy candidates and allowed us to make the first inferences of the star-formation rate density at  $z = 9 - 10$  (Zitrin et al. 2014; Ishigaki et al. 2015; Oesch et al. 2015). Moreover, the magnifications produced by lensing enables us to reach intrinsically faint, low-mass galaxies. Thanks to carefully calibrated lensing models (e.g., Meneghetti et al. 2017), subtraction of intracluster light (Merlin et al. 2016; Livermore et al. 2017), and calibration of the measured sizes (Kawamata et al. 2015; Bouwens et al. 2017a), there has been substantial progress in deriving both the prevalence of intrinsically faint, lower-luminosity galaxies and the faint-end slope of the ultraviolet (UV) luminosity function (LF) (Atek et al. 2014, 2015a; Alavi et al. 2016; Livermore et al. 2017; Bouwens et al. 2017b).

In addition, it is important to find highly magnified galaxies in order to detect intrinsically faint UV metal lines, such as C IV  $\lambda 1548 \text{ \AA}$  (Stark et al. 2014, 2015a) and C III]  $\lambda 1909 \text{ \AA}$  (Rigby et al. 2015; Stark et al. 2014, 2015b, 2017; Mainali et al. 2017) at high redshift. These UV lines can now be seen out to  $z=6-7$ , including intrinsically faint Lyman- $\alpha$  (Hoag et al. 2017). It is imperative to detect these faint metal lines not only because they help us to deduce the shape of the ionizing spectra, but they also allow us to spectroscopically confirm the redshifts of galaxies in the epoch of reionization, given that the Lyman- $\alpha$  line becomes completely opaque to the line-of-sight neutral intergalactic medium (Stark et al. 2010; Schenker et al. 2012; Tilvi et al. 2013; Pentericci et al. 2014).

The rich history of using strong lensing systems to study in detail  $z \approx 4 - 7$  galaxies (Franx et al. 1997; Bradley et al. 2008; Zitrin et al. 2012; Jones et al. 2013; Kawamata et al. 2015) and reveal the  $z \approx 8 - 11$  population (Zheng et al. 2012; Coe et al. 2013; Bouwens et al. 2014; Zitrin et al. 2014; McLeod et al. 2016; Ishigaki et al. 2015, 2017) was the motivation for the Reionization Lensing Cluster Survey (RELICS; Coe et al. in prep). RELICS is a 190-orbit *Hubble Space Telescope* (*HST*) Treasury Program designed to build off of the success of other *HST* lensing surveys like CLASH and the HFF, and take advantage of clusters with existing *HST*/ACS imaging and/or data suggesting exceptionally high cluster masses. In short, the survey targeted 41 massive galaxy clusters selected by the *Planck* survey (Planck Collaboration et al. 2016; Robertson et al. 2015) to be excellent lensing systems. This survey is timely in advance of the *James Webb Space Telescope* (*JWST*) 2018 launch date, as *JWST* was not designed to be a wide-field survey telescope and will benefit from existing high-

redshift candidates. We present here the first results of the RELICS program, providing to the community all of its high-redshift candidates found to-date.

This paper is organized as follows. In Section 2, we summarize our observations, redshifts, and selection. In Section 3 we describe our resulting magnitudes of the objects in our sample, and present the SEDs and images of bright sources. In Sections 4 we discuss our conclusions and future work. Throughout, we assume concordance cosmology using  $H_0 = 70 \text{ km s}^{-1} \text{ Mpc}^{-1}$ ,  $\Omega_{\text{M},0} = 0.3$  and  $\Omega_{\Lambda,0} = 0.7$ . All magnitudes quoted here are measured with respect to the AB system,  $m_{\text{AB}} = 31.4 - 2.5 \log(f_{\nu}/1 \text{ nJy})$  (Oke & Gunn 1983).

## 2. DATA, REDSHIFTS, AND SAMPLE SELECTION

### 2.1. RELICS Cluster Selection and HST Photometry

The RELICS clusters were selected by a combination of their cluster mass and pre-existing ACS imaging. From the most massive Planck clusters (identified by their Sunyaev Zel'dovich cluster mass; Planck Collaboration et al. 2016), we first selected the 8 most massive clusters that had *HST*/ACS but not WFC3 infrared imaging, and another 13 massive Planck clusters that had no *HST* or *Spitzer* imaging at all. The 20 other RELICS clusters are selected from known strong lenses that have already have *HST* optical imaging. We also note that seven of the RELICS clusters can be found in the MACS program by Ebeling et al. (2001). We initially inferred the cluster lensing strengths from a variety of sources, including their X-ray mass (MCXC; Piffaretti et al. 2011; Mantz et al. 2010), weak lensing mass (Sereno 2015; Applegate et al. 2014; von der Linden et al. 2014; Umetsu et al. 2014; Hoekstra et al. 2015), SDSS data (Wong et al. 2013; Wen et al. 2012), and other SZ mass estimates (Bleem et al. 2015; Hasselfield et al. 2013). Further details on the cluster selection can be found by Cerny et al. (2017) and Coe et al. (in prep).

We target all 41 clusters with two orbits of WFC3/IR comprising observations in F105W, F125W, F140W, and F160W. Five clusters are observed with an additional pointing, for a total of 46 IR fields. We take advantage of existing archival ACS imaging, and for the 18 clusters without any F435W, F606W, and F814W we observe 3 orbits total, with one orbit per filter. For the ACS imaging we also observe WFC3/IR fields in parallel, which are not explored in this work. The observations are split into two epochs separated by about a month to facilitate variability search. Twenty additional orbits were allocated for variability Target of Opportunity follow up.

The SExtractor (version 2.8.6; Bertin & Arnouts 1996) object selection and *HST* photometry are described by Coe et al. (in prep), which we summarize here. First, we use the AstroDrizzle package (Gonzaga & et al. 2012) to combine all sub-exposures from each filter. After aligning the filters to the same pixel frame, we correct the absolute astrometry with the Wide-field Infrared Survey Explorer (WISE) point source catalog (Wright et al. 2010). Then, we construct the final drizzled images by sampling the point-spread functions of both the ACS and WFC3/IR cameras in 30 milli-arcsecond (mas)/pixel and 60 mas/pixel scales.

Finally, RELICS produces the full photometric catalogs of each cluster field. In this work, we use the cata-

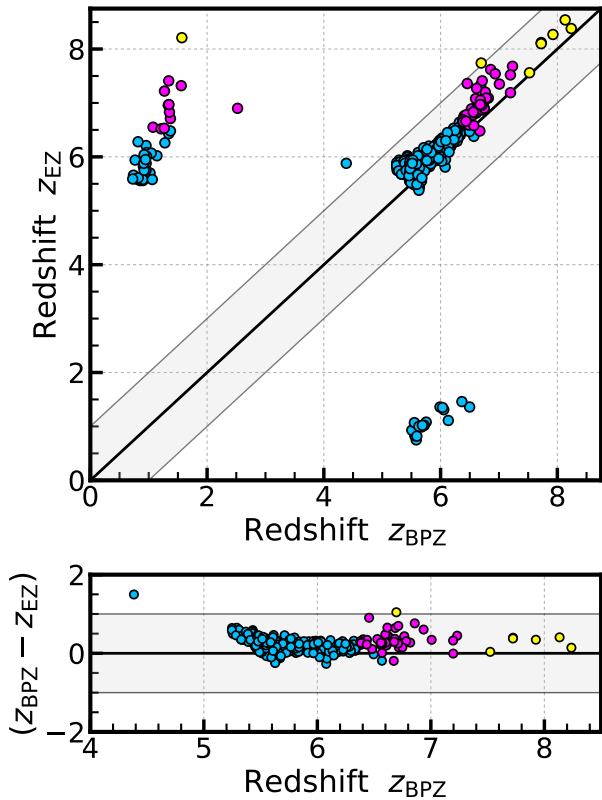


**Figure 1.** Comparison of EAZY and BPZ photometric redshifts for our high- $z$  sample. The grey regions show  $\Delta z = \pm 1$ . Objects with large differences are due to one code preferring a  $z \sim 1$  dusty or high EW nebular emission line galaxy. Both EAZY and BPZ otherwise agree within typical photometric-redshift uncertainties at these redshifts.

logs based on a detection image comprised of the 60 mas weighted stack of all WFC3/IR imaging. The source extraction was performed with SExtractor in dual-image mode, with fluxes measured within the isophotal apertures. All fluxes are corrected for Galactic extinction assuming the extinction law by Schlafly & Finkbeiner (2011).

## 2.2. RELICS *Spitzer* Photometry

In addition to the new *HST* imaging, RELICS also has tandem *Spitzer* IRAC programs (PI Bradač, PI Soifer) totaling 390 hours. The IRAC 3.6  $\mu\text{m}$  and 4.5  $\mu\text{m}$  bands are especially helpful when calculating photometric redshifts as their data helps to distinguish between  $z > 5$  galaxies and dusty  $z \sim 2-3$  galaxies. As these data are still being processed, we do not yet employ the full *Spitzer* photometry in the sample selection of this work. We will present the full RELICS *Spitzer* photometric catalogs in a future work.

## 2.3. Photometric Redshifts

In this work, we utilize two different photometric-redshift fitting codes to identify high- $z$  galaxy candidates: the Bayesian photometric redshift code (BPZ v1.99.3; Benítez 2000; Benítez et al. 2004; Coe et al. 2006) and BPZ and the Easy and Accurate Z (photometric redshifts) from Yale EAZY (Brammer et al. 2008). Both are similar in that they fit a variety of empirically driven

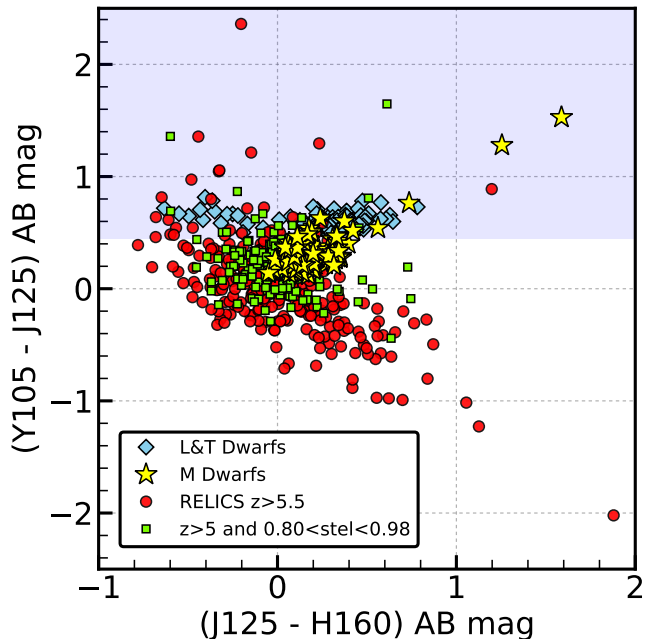


**Figure 2.** The YJH colors of the RELICS high- $z$  galaxy candidates. The red circles and green squares are objects with  $z_{\text{phot,Max}} > 5.5$ , where the latter are those with high stellarity ( $> 0.8$ ). The blue diamonds and yellow stars are colors of known L&T and M dwarfs respectively, taken from IRTF observed spectral library (Cushing et al. 2005; Rayner et al. 2009). Most of the high-redshift galaxy candidates with high stellarity (green squares) have colors dissimilar from the dwarf stars. We remove all objects with  $z_{\text{phot,Max}} > 5.5$ ,  $(Y - J) > 0.45$ , and stellarity  $> 0.8$ , which correspond to the green squares in the blue shaded region.

galaxy spectral energy distributions (SEDs) to the data and find the template and redshift that best matches the object. Photometric-redshift codes are fundamentally similar to color-color selections in their identification of high-redshift galaxies: they use input photometric bands to identify a sharp increase in flux between two bands, and leverage with data at other wavelengths to infer the presence of the Lyman break (due to the line-of-sight neutral intergalactic medium absorbing photons at rest wavelengths shorter than 1216  $\text{\AA}$ ), the Balmer break (which becomes more pronounced in older stellar populations), or strong nebular emission lines. The main difference between photometric redshifts and color-color selections is that the former is able to assign a likelihood at each redshift by comparing the photometry to a library of redshifted stellar population templates. We describe below the two photometric-redshift codes and their implementation.

### 2.3.1. BPZ redshifts

First, we derived photometric redshifts using BPZ. BPZ is based on  $\chi^2$ -fitting by comparing the observed fluxes to PEGASE (Fioc & Rocca-Volmerange 1997) SED templates. BPZ employs a Madau (1995) intergalactic medium attenuation, which accentuates the Lyman break. The default templates span a range of rest-frame UVJ colors, and are combined to produce SEDs with synthetic spectra similar to the high-quality spectra of most galaxies (e.g., with  $\leq 1\%$  outliers, see Coe et al. 2013), including red dusty star-forming galaxies. We use the

default BPZ templates for fitting redshifts in this work.

Besides the choice of template SEDs, perhaps the biggest assumption in a given photometric redshift code is the handling of the prior. In BPZ, the Bayesian prior  $P(z, t|m_0)$  is a redshift and magnitude ( $m_0$ )-dependent prior applied to each template  $t$ , so as to down-weight the likelihood of, for example, the unphysical presence of bright elliptical galaxies at very high ( $z > 4$ ) redshifts. As we discuss further in the following section, the exact prior for  $z > 6$  is a poorly constrained function given that the population of intrinsically faint galaxies of different types is unknown. Nevertheless, we found that for BPZ some simple prior must be assumed to avoid an overpopulation of quiescent-like SEDs at high redshift. With this prior, we calculate the posterior  $P(z)$  for every object in each RELICS field and define our accepted BPZ redshifts as the redshift corresponding to the mode of the final probability function.

### 2.3.2. EAZY redshifts

Similar to BPZ, the EAZY photometric-redshift code creates the redshift likelihood density function ( $P(z)$ ) by computing the  $\chi^2$  between the observed fluxes and a linear combination of redshifted empirical SED templates. EAZY includes 7 default templates from PEGASE stellar population models (Fioc & Rocca-Volmerange 1997), a red, highly dust-obscured galaxy (Maraston 2005), and an extreme, high-equivalent width (EW) nebular emission line galaxy (Erb et al. 2010) (see the Appendix Figure 14 to compare the rest-frame  $UVJ$  and observed-frame  $YJH$  colors of EAZY and BPZ templates).

While the  $P(z)$  can be weighted by a  $K$ -band luminosity prior, we choose to assume a flat prior for several reasons. First, we do not wish to bias ourselves against high- $z$  galaxies that are unnaturally bright due to high lensing magnification. Second, the priors at the highest redshifts are poorly calibrated, as we are only just exploring the completeness at these  $z > 6$  redshifts. More importantly, we input model fluxes of  $z > 6$  galaxies with typical data uncertainties and attempted to recover the redshift using the default EAZY prior. We found that the default prior tends to systematically prefer the high-EW low- $z$  solution over high- $z$  solutions. A better estimation of the correct prior for each code may become more clear when the photometric-redshifts are improved with the inclusion of the Spitzer photometry.

For any photometric-redshift code, most uncertainty at  $z > 4$  redshifts comes from the degenerate solutions with red,  $z \sim 1 - 2$  galaxies with either high dust obscuration or evolved stellar populations. In the Appendix, we show the WFC3  $YJH$  color tracks with increasing redshift to show how high- $z$  galaxy colors are similar to  $z = 1 - 2$  red galaxies. A slight preference to one of these degenerate solutions, due to the different assumed templates, is the primary cause for the few cases where BPZ and EAZY redshifts seem to differ by  $\Delta z > 1$ .

To be sure we were not omitting a population of high- $z$  galaxies that systematically preferred the low- $z$  degenerate solution over the high- $z$  (in either code), we visually inspected all galaxies by their morphologies, individual band images, stacked WFC3/IR and ACS images, SEDs, and  $P(z)$  distributions for all objects with appreciable likelihood at high redshift,  $P(z > 4) > 40\%$ . We concluded that there were no convincing high- $z$  candidates

(following the visual inspection parameters described in S 2.4 below) that did not have a maximal likelihood redshift or a median  $P(z)$  redshift of  $z > 5.5$  in at least one of the EAZY or BPZ fitting results.

To construct our sample of high- $z$  galaxy candidates we ultimately choose to adopt the average redshift between the BPZ and BPZ estimates unless they differ by  $\Delta z > 1$  in which case we adopt the higher redshift solution. While this list will inevitably contain some low- $z$  contaminants, we aim to further validate the sample by a close inspection of the available *Spitzer* photometry or with follow-up observations.

### 2.4. High- $z$ Sample Selection

The RELICS catalogs contain a combined total of over 76,000 sources. From these sources we identify 2,425 objects with appreciable likelihood at  $z > 5.5$ ,  $P(z > 5.5) > 40\%$ . After initial visual inspections, we found that galaxies only appeared to be bona-fide candidates (that is, S/N > 3, small sizes, and detections in individual infrared bands) if at least one of the photometric-redshift fitting codes had a median or peak likelihood at  $z > 5.5$ . This lead us to adopting a single redshift per object in order to produce a complete candidate list. We took advantage of our use of two independent photometric redshift codes by assigning the redshift of each object to be the average of the BPZ and BPZ estimates unless they differ by  $\Delta z > 1$  in which case we adopted the higher redshift solution. We note that the BPZ and EAZY redshifts are in approximate agreement ( $|\Delta z| < 1$ ) for 87% of the sample. We then selected objects with  $z_{\text{phot}} > 5.5$  to reduce the initial candidate list to 1,337 objects. We further refined the sample by selecting galaxies with an F160W detection greater than  $3\sigma$  as adopted by Bradley et al. (2014), reducing to 841 objects.

With any high- $z$  sample, we must be diligent to remove contamination by foreground Galactic stars. L, T, and M dwarf stars and brown dwarfs have similar broadband IR colors as  $z = 6 - 7$  galaxies (Tilvi et al. 2013). The SExtractor “stellarity” parameter is one potentially discriminatory way of doing so, with generally effective discriminatory power to  $J < 25$  or  $J < 26$  reported by Finkelstein et al. (2015) and Bouwens et al. (2015), respectively, but with lesser reliability fainter than these levels. This is exacerbated in lensing fields where high stellarity objects could be stars or strongly lensed high- $z$  galaxies. To mitigate this problem, we use both stellarity and a color selection to reduce our stellar contamination.

Figure 2 shows the  $YJH$  colors of the RELICS high- $z$  sample compared to observed spectra of L, T, and M dwarf stars (Cushing et al. 2005; Rayner et al. 2009). We outright remove objects with a stellarity  $\geq 98\%$  (111 objects) because these objects have very low FWHM ( $< 0.25''$ ) and magnitudes systematically brighter than expected for typical lensing magnifications (mean of 22.8 mag, well above the distribution of magnitudes of lensed  $z > 6$  galaxies from CLASH; see Bradley et al. (2014)). Fig. 2 shows that the colors of most objects at intermediate stellarity (80-98%) are dissimilar to stellar colors. Until full lens models are available for each field, we do not wish to rule out a population of highly lensed, compact galaxies, especially given recent estimates for the size of  $2 < z < 8$  lensed galaxies in the HFF (Vanzella et al. 2016, 2017; Bouwens et al. 2017a). We

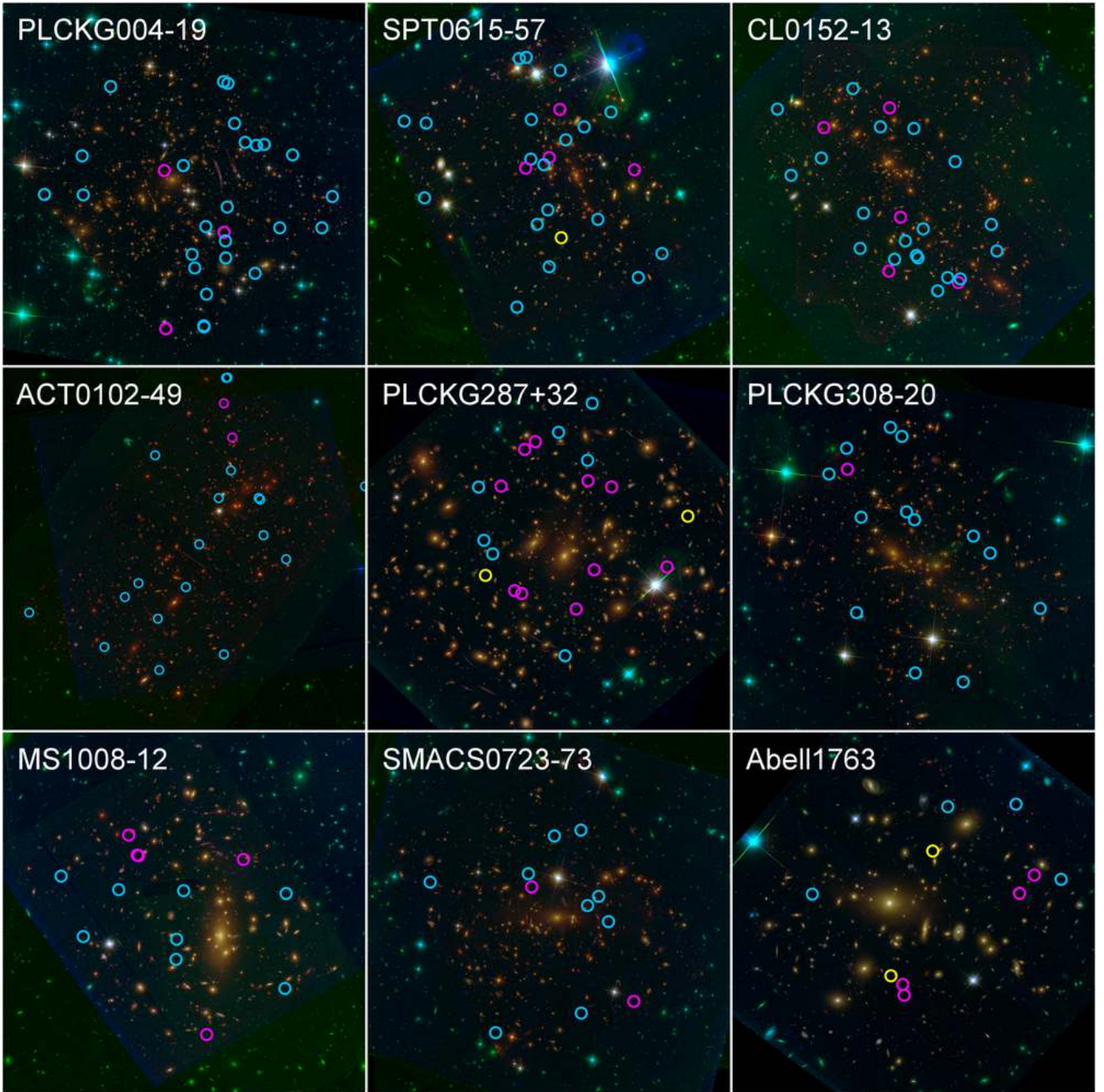


**Figure 3.** Color images of the top nine clusters after rank ordering by the number of  $z > 5.5$  galaxies they produce (excluding RXS0603+42 whose two WFC3/IR pointings are separated by  $6'$ ). North is up and east is to the left. The images are scaled to  $3'.25 \times 3'.25$ , except for ACT0102-49 which is  $4'.25 \times 4'.25$ . The cyan, magenta, and yellow circles mark the location of the  $z \sim 6$ , 7, and 8 candidate galaxies respectively.

therefore make the modest selection to only omit high- $z$  objects that satisfy both high stellarity (80-98%) and  $(Y - J) > 0.45$  colors.

Finally, we conduct an extensive visual inspection of all remaining candidates, observing their detection in each band, ACS and WFC3 summed images, SExtractor segmentation maps, and the best-fit SEDs and  $P(z)$  from both BPZ and EAZY. The samples were cleared of diffraction spikes, misidentified parts of larger galaxies, stars, candidates too close to the infrared detector edge, tran-

sients between epochs, and other image artifacts. For high- $z$  galaxies that were obviously spatially distorted due to lensing, we remove the duplicate segmentations (18 in total) and retain the brightest segment to represent the object in the catalog. In total we find 255 galaxies at  $z \sim 6$ , 57 at  $z \sim 7$ , and 8 at  $z \sim 8$ .

### 3. RESULTS

Figure 3 shows RGB color images of the top nine high- $z$ -producing fields (excluding RXS0603+42, whose two

**Table 1**  
High- $z$  Number Counts Per Cluster

| Cluster      | R.A.<br>(J2000) | Dec.<br>(J2000) | Cluster<br>Redshift | Planck Mass<br>( $10^{14}M_{\odot}$ ) | $N_{\text{total}}$ | $N_{z=6}$ | $N_{z=7}$ | $N_{z=8}$ |
|--------------|-----------------|-----------------|---------------------|---------------------------------------|--------------------|-----------|-----------|-----------|
| PLCKG004-19  | 19:17:4.50      | -33:31:28.5     | 0.520               | 10.36                                 | 28                 | 25        | 3         | 0         |
| SPT0615-57   | 06:15:54.2      | -57:46:57.9     | 0.972               | 6.77                                  | 25                 | 19        | 4         | 1         |
| CL0152-13    | 01:52:42.9      | -13:57:31.0     | 0.833               | . . .                                 | 24                 | 19        | 5         | 0         |
| ACT0102-49   | 01:02:53.1      | -49:14:52.8     | 0.870               | 10.75                                 | 21                 | 19        | 2         | 0         |
| PLCKG287+32  | 11:50:50.8      | -28:04:52.2     | 0.39                | 14.69                                 | 19                 | 7         | 10        | 2         |
| PLCKG308-20  | 15:18:49.9      | -81:30:33.6     | 0.480               | 10.32                                 | 14                 | 13        | 1         | 0         |
| MS1008-12    | 10:10:33.6      | -12:39:43.0     | 0.306               | 4.94                                  | 13                 | 8         | 5         | 0         |
| RXS0603+42   | 06:03:12.2      | +42:15:24.7     | 0.228               | 10.76                                 | 13                 | 13        | 0         | 0         |
| SMACS0723-73 | 07:23:19.5      | -73:27:15.6     | 0.390               | 8.39                                  | 11                 | 9         | 2         | 0         |
| Abell1763    | 13:35:18.9      | +40:59:57.2     | 0.228               | 8.13                                  | 10                 | 4         | 4         | 2         |
| MACS0553-33  | 05:53:23.1      | -33:42:29.9     | 0.430               | 8.77                                  | 9                  | 5         | 3         | 1         |
| MACS0257-23  | 02:57:10.2      | -23:26:11.8     | 0.505               | 6.22                                  | 9                  | 8         | 1         | 0         |
| RXC0600-20   | 06:00:09.8      | -20:08:08.9     | 0.460               | 10.73                                 | 8                  | 7         | 1         | 0         |
| MACS0025-12  | 00:25:30.3      | -12:22:48.1     | 0.586               | . . .                                 | 7                  | 6         | 1         | 0         |
| Abell2163    | 16:15:48.3      | -06:07:36.7     | 0.203               | 16.12                                 | 7                  | 6         | 1         | 0         |
| Abell1758    | 13:32:39.0      | +50:33:41.8     | 0.280               | 8.22                                  | 6                  | 6         | 0         | 0         |
| RXC0018+16   | 00:18:32.6      | +16:26:08.4     | 0.546               | 9.79                                  | 6                  | 6         | 0         | 0         |
| Abell520     | 04:54:19.0      | +02:56:49.0     | 0.203               | 7.80                                  | 6                  | 5         | 1         | 0         |
| MACS0308+26  | 03:08:55.7      | +26:45:36.8     | 0.356               | 10.76                                 | 6                  | 6         | 0         | 0         |
| RXC0911+17   | 09:11:11.4      | +17:46:33.5     | 0.505               | 6.99                                  | 6                  | 4         | 1         | 1         |
| Abells295    | 02:45:31.4      | -53:02:24.9     | 0.300               | 6.78                                  | 6                  | 4         | 1         | 1         |
| Abell665     | 08:30:57.4      | +65:50:31.0     | 0.182               | 8.86                                  | 5                  | 5         | 0         | 0         |
| Abell3192    | 03:58:53.1      | -29:55:44.8     | 0.425               | 7.20                                  | 5                  | 2         | 3         | 0         |
| PLCKG209+10  | 07:22:23.0      | +07:24:30.0     | 0.677               | 10.73                                 | 5                  | 5         | 0         | 0         |
| Abell2537    | 23:08:22.2      | -02:11:32.4     | 0.297               | 5.52                                  | 5                  | 5         | 0         | 0         |
| SPT0254-58   | 02:54:16.0      | -58:57:11.0     | 0.438               | 9.69                                  | 4                  | 3         | 1         | 0         |
| RXC0142+44   | 01:42:55.2      | +44:38:04.3     | 0.341               | 9.02                                  | 4                  | 3         | 1         | 0         |
| Abell1300    | 11:31:54.1      | -19:55:23.4     | 0.307               | 8.97                                  | 4                  | 2         | 2         | 0         |
| MACS0159-08  | 01:59:49.4      | -08:50:00.0     | 0.405               | 7.20                                  | 4                  | 3         | 1         | 0         |
| MACS0035-20  | 00:35:27.0      | -20:15:40.3     | 0.352               | 7.01                                  | 4                  | 3         | 1         | 0         |
| WHL0137-08   | 01:37:25.0      | -08:27:25.0     | 0.566               | 8.93                                  | 4                  | 4         | 0         | 0         |
| Abell697     | 08:42:58.9      | +36:21:51.1     | 0.282               | 11.0                                  | 4                  | 4         | 0         | 0         |
| PLCKG138-10  | 02:27:06.6      | +49:00:29.9     | 0.702               | 9.48                                  | 3                  | 2         | 1         | 0         |
| PLCKG171-40  | 03:12:56.9      | +08:22:19.2     | 0.270               | 10.71                                 | 3                  | 3         | 0         | 0         |
| RXC0032+18   | 00:32:11.0      | +18:07:49.0     | 0.396               | 7.61                                  | 3                  | 2         | 1         | 0         |
| RXC0232-44   | 02:32:18.1      | -44:20:44.9     | 0.284               | 7.54                                  | 3                  | 3         | 0         | 0         |
| RXC0949+17   | 09:49:50.9      | +17:07:15.3     | 0.383               | 8.24                                  | 3                  | 3         | 0         | 0         |
| RXC1514-15   | 15:15:00.7      | -15:22:46.7     | 0.223               | 8.86                                  | 2                  | 2         | 0         | 0         |
| RXC2211-03   | 22:11:45.9      | -03:49:44.7     | 0.397               | 10.5                                  | 2                  | 2         | 0         | 0         |
| Abell2813    | 00:43:25.1      | -20:37:14.8     | 0.292               | 8.13                                  | 2                  | 2         | 0         | 0         |
| MACS0417-11  | 04:17:33.7      | -11:54:22.6     | 0.443               | 12.25                                 | 0                  | 0         | 0         | 0         |

WFC3/IR pointings are separated by  $6'$ ), and the overlaid position of each high- $z$  candidate. These images show that our candidate high- $z$  galaxies are not clustered around the edges of the IR detector, thanks to our visual screening of every candidate. [Cerny et al. \(2017\)](#) conducted an analysis of the first five RELICS clusters, which span the range of masses and redshifts of the clusters in the full program. They found that these five clusters had lensing efficiencies of similar strength to the Frontier Fields. In future works, we will publish the lens models and magnifications of all 41 clusters, which will allow us to explore the lensed counter images.

The breakdown of the number of galaxies in each cluster and each redshift bin are shown in Table 1. Figure 4 displays these number counts per cluster as a histogram. Clearly, some clusters produce many more high- $z$  can-

didates than others, even after accounting for the five clusters that have additional WFC3/IR pointings. For example, the top  $\approx 12\%$  of the high- $z$  producing clusters contain as many candidates (almost a third of the entire  $z > 5.5$  sample) as the bottom 50% of the clusters. Fig. 4 also shows that there appears to be little to no correlation between the ability of a cluster to produce high- $z$  sources and its cluster mass, at least at these high masses. However, a weak correlation exists with the number of high- $z$  candidates and the cluster redshift. However, there may be several reasons for why some clusters are better at producing high- $z$  sources than others, such as a dependence on the cluster mass distribution and concentration, the latter of which is expected to correlate with dark matter halo mass ([Bullock et al. 2001](#); [Neto et al. 2007](#); [Umetsu et al. 2014](#)). In addition, there may be sample variance

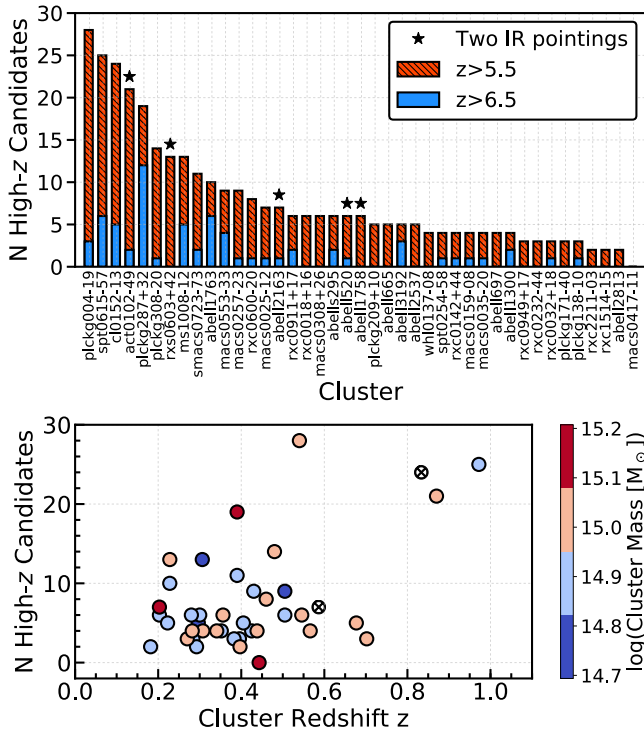


**Figure 4.** The number of high- $z$  candidates for each cluster field observed by RELICS. *Top:* Histograms of the number of  $z > 5.5$  candidate galaxies (solid blue and hatched red) and number of  $z > 6.5$  candidates (solid blue only). The five clusters with two WFC3/IR pointings are noted with the solid stars. Some clusters produce considerable numbers of high- $z$  candidates compared to others. *Bottom:* The number of high- $z$  candidates per cluster as a function of the cluster redshift. The blue-to-red colors portray the cluster mass ( $M_{500}$ ) from Planck Collaboration et al. (2016), where the crossed circles show the two clusters without mass estimates. There is a weak correlation between the cluster redshift and the cluster’s ability to produce many high- $z$  galaxy candidates, and little correlation with the cluster mass.

in the alignment of background galaxies. A comprehensive exploration of cluster lensing strength will require a comparison between the lens models from all RELICS clusters.

### 3.1. Magnitude Distribution

Figure 5 shows distribution of F160W  $H$ -band magnitude for the RELICS high- $z$  galaxies compared to that of the CLASH survey. RELICS produces the same, if not more, high- $z$  galaxies at a given redshift and magnitude than the first 360 orbits of CLASH. The comparison to CLASH is important because although RELICS viewed roughly twice as many clusters as CLASH, the infrared depth was much shallower per cluster (typically a factor of 4 less IR exposure time than CLASH) and the program used roughly a third as many orbits to complete (compared to the total 524 *HST* orbits by CLASH). Fig. 5 also highlights the abundance of bright  $m_{\text{AB}} < 26$  candidates at a given redshift, which presents a promising sample for follow-up spectroscopy.

Figure 6 shows the  $H$ -band magnitude of the RELICS high- $z$  candidates as a function of redshift compared to several large surveys including CANDELS (Bouwens et al. 2015; Finkelstein et al. 2015), the HFF (Ishigaki et al. 2017), CLASH (Bradley et al. 2014), Ultra-VISTA (Bowler et al. 2017), and BoRG/HIPPIES (Bradley et al.

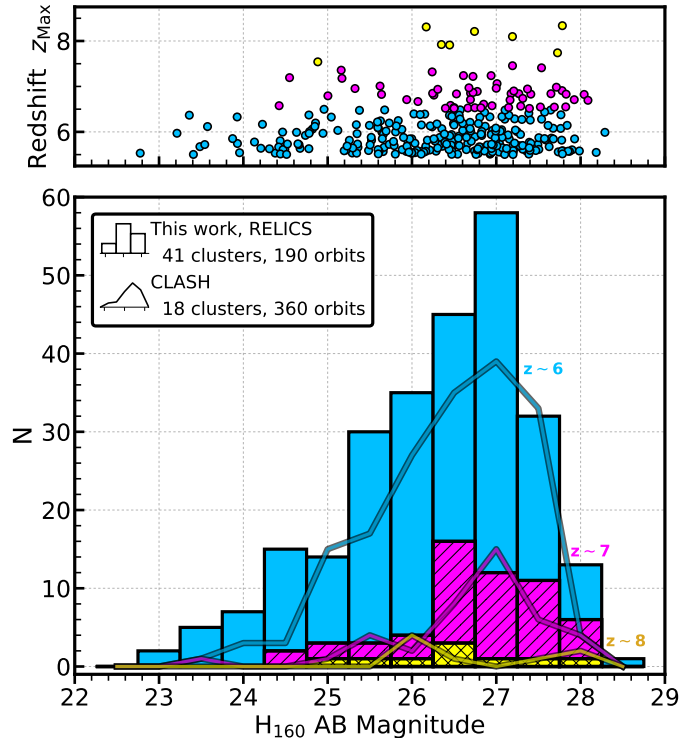


**Figure 5.** The distribution of WFC3 F160W  $H$ -band observed (lensed) magnitude for our  $z \sim 6, 7$ , and 8-10 RELICS samples in solid blue, left-hatched magenta, and right-hatched yellow histograms. The curves show the distribution of  $z \sim 6, 7$ , and 8-10 galaxies (blue, magenta, and yellow, respectively) from the first 18 clusters and 360 orbits of CLASH (Bradley et al. 2014). The above panel shows the photometric redshifts of individual RELICS galaxies as a function of their magnitude. RELICS produces a similar magnitude distribution of high- $z$  galaxies as CLASH.

2012; Schmidt et al. 2014; Calvi et al. 2016). RELICS produces galaxies that are among the brightest at a given redshift over  $z \sim 6$  to  $z \sim 8$ , comparable to these much wider and deeper programs. We highlight this comparison to emphasize the efficiency of targeting strong lensing fields to produce high- $z$  candidates, which is especially relevant as the costly overheads of *JWST* make the telescope more efficient at smaller area surveys.

Finally, Figure 7 displays the number density of galaxies in bins of magnitude over  $z = 6-8$ . We assume an area of 4.5 arcmin<sup>2</sup> for each of the 46 WFC3/IR pointings for a total survey area of 207 arcmin<sup>2</sup>. The actual area will change after lens models determine the magnification maps and the effective area covered for each cluster, although typical areas from CLASH range between 4.3 – 4.8 arcmin<sup>2</sup> per cluster field. Nevertheless, we observe a clear excess in number density at the  $z \sim 6$  and 7 bright magnitudes compared to unlensed fields. We note that the drop off at fainter magnitudes ( $m_{\text{AB}} > 26.5$ ) is due to survey incompleteness.

To provide a baseline comparison for our results, we make use of a LF with a double power-law fit to a comprehensive set of  $z \sim 6, 7$ , and 8 results from the literature (see Appendix). A double power-law has been found to work well in representing the extreme bright-end shape of the UV LF (Bowler et al. 2014, 2015; Ono et al. 2017; Stefanon et al. 2017). By comparing the bright end of our results from RELICS against that of a double-law LF, we

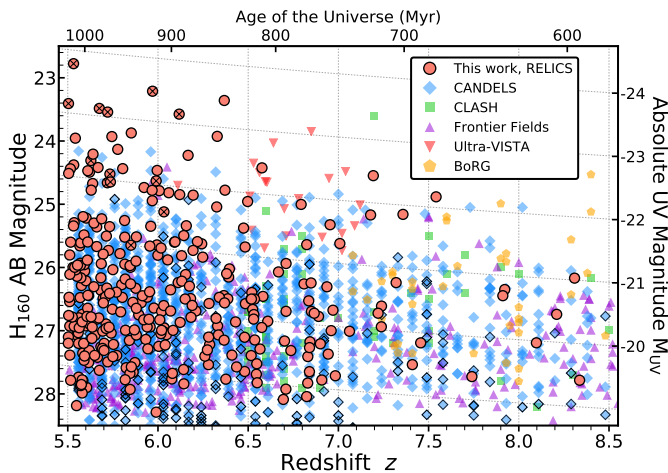


**Figure 6.** The  $H$ -band magnitude as a function of redshift. The high- $z$  galaxy candidates from RELICS are shown as salmon-colored circles. Circles filled with an “X” mark candidates from the cluster field RXS0603+42, which is at a low Galactic latitude ( $b \approx 10^\circ$ ) and therefore has a potentially higher stellar contamination. The green squares are galaxies from CLASH (Bradley et al. 2014), the purple upwards-triangles from the Frontier Field (Ishigaki et al. 2017), the red downwards-triangle from Ultra-VISTA (Bowler et al. 2017), the blue diamonds from CANDELS (Bouwens et al. 2015) (outlined diamonds are from the HUDF; see also Finkelstein et al. 2015), and the orange pentagons from BoRG/HIPPIES (Bradley et al. 2012; Schmidt et al. 2014; Calvi et al. 2016). Gray background lines follow the conversion from apparent magnitude to absolute UV magnitude. RELICS finds some of the brightest known galaxies at a given redshift over  $z \sim 8$  to  $z \sim 6$ .

aim to show that the number density boost from lensing we observe exceeds even the expectation from the double-law LF, which already exhibits a much larger number of sources than a LF with a Schechter (Schechter 1976) form. As a second baseline comparison for our results, we also show the expectations from the literature-averaged Schechter function results from Finkelstein (2016) which features fewer sources at the extreme bright-end due the bright-end shape of the Schechter function, but overall is very similar at luminosities less than  $2L^*$ .

Next, we apply typical CLASH cluster-lensing magnifications to model how the number densities of the true luminosity function appear under the effects of cluster lensing. We only show the effects of lensing on the double-law LF, but we note that forms of the LF produce a similar lensed shape. Comparing the lensed luminosity function to the binned number densities of RELICS and CLASH, we find they agree with the prediction well at  $z \sim 6$ , and that both surveys tend to underproduce from the expected number of sources at  $z \sim 7$  and 8. It is hard to speculate if this is due to an actual bright-end decline in number density at higher redshifts, as seen by Bowler et al. (2017), until we conduct full completeness simulations and lens modeling of all 41 RELICS clusters and consider the effects of cosmic variance.

### 3.2. Exceptionally Bright Sources

The RGB image stamps of the brightest 40 galaxy candidates from RELICS for  $z \sim 6$  and 7, and all candidates for  $z \sim 8$  are shown in Figures 8, 9, 12 respectively. In particular, we note the third brightest  $z \sim 6$  candidate, MACS0308-904, which has been clearly arced by the effects of lensing and is likely highly magnified. Not all

highly magnified galaxies will also be arced, which makes it very difficult with the current data to distinguish between stellar contaminants and high- $z$  galaxies among the brightest candidates. We have already attempted to remove stellar contaminants by a combination of YJH colors and stellarity (Fig. 2 and § 2.4). In addition, we checked the brightest candidates in our samples with the Galactic latitude of their cluster field. We find that  $\approx 6$  of our brightest  $z \sim 6$  candidates come from a cluster field with relatively low Galactic latitude (RXS0603+42, at  $b = 9.7^\circ$ ). We specially note these objects in Fig. 6 and their images and SEDs can be inspected in Figs 8 and 10. Besides this one cluster, we see no correlation between the number or brightness of high- $z$  candidates and the Galactic latitude of the cluster fields. We anticipate a deeper exploration of contaminants in the future using lensing magnifications, *Spitzer* photometry, and/or spectroscopic redshifts.

Following the same plotting grid of the image stamp figures, the SEDs of the brightest candidates and their photometric-redshift template fits for BPZ and EAZY are shown in Figures 10, 11, 13 respectively. Several objects appear to have red SEDs, but we caution that this is because the rest-frame optical is unconstrained prior to the inclusion of *Spitzer*, which makes estimates of physical parameters like stellar mass unreliable. In Tables 2, 3, and 4 we make available the  $z = 6, 7,$  and 8 candidate galaxies from the RELICS survey. We include both the photometric estimates of EAZY and BPZ. The full tables will be made available online.

## 4. CONCLUSIONS

We present the candidate high- $z$  galaxies first estimated from RELICS, an *HST* Treasury Program observing 41 galaxy clusters. We use two independent photometric-redshift fitting codes to determine the redshifts of each galaxy. We also compare the colors of the candidates to those of known dwarf stars, and apply a color selection to remove the most likely contaminants. Furthermore, we conduct an extensive visual inspection of all potential high- $z$  candidates, cleaning the sample of diffraction spikes, misidentified parts of larger galaxies, stars, spurious noise close to the infrared detector edge, transients between epochs, and other image artifacts.

The final sample of candidate high- $z$  galaxies is of comparable size to the CLASH program, despite being significantly more shallow. In particular, we identify several candidates that are among the brightest galaxies at  $z \sim 6$  to 8, as compared to much deeper and wider area surveys. This presents a promising sample for follow-up spectroscopy to study the nebular ionization conditions, Lyman- $\alpha$  emission, and other galaxy properties into the epoch of reionization.

Finally, we compare the number of galaxies found to the predictions from lensed luminosity functions. We find that our  $z \sim 6$  sample agrees with expectations from the literature luminosity functions, while  $z \sim 7$  and 8 begin to under-produce the number of candidates compared to expectations from current luminosity functions. The paucity of galaxies from the higher redshift samples could imply the start of an accelerated bright-end evolution in the UV LF, although we await the completion of the *Spitzer* data and completeness simulations for further confirmation.



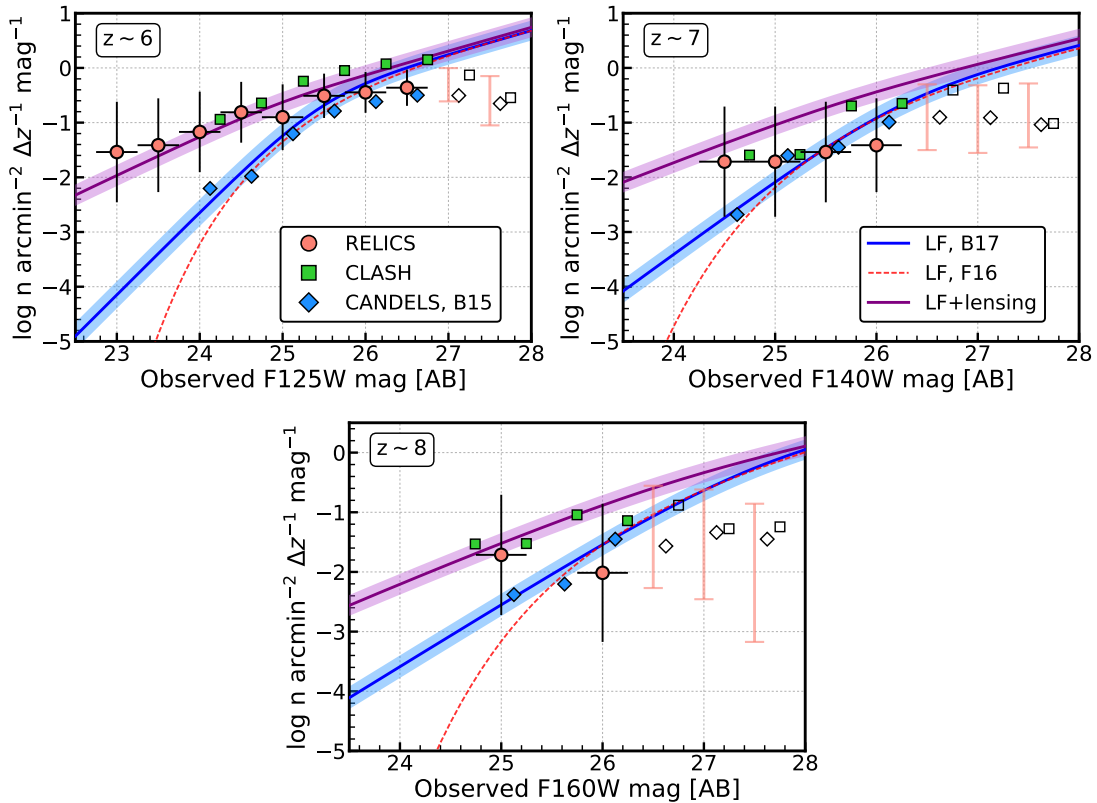


**Figure 7.** The number density of galaxies per magnitude and redshift bin at  $z \sim 6, 7$  and  $8$ . The observed number densities in the 41-cluster RELICS samples are shown as salmon-colored circles, with their  $1\text{-}\sigma$  Poissonian uncertainties. The green squares are the observed number densities seen in CLASH by Bradley et al. (2014) and the blue diamonds are those seen in CANDELS by Bouwens et al. (2015). The blue and red-dashed curves represent the Double-Power-Law and Schechter fits to a suite of published luminosity function results (Oesch et al. 2012; Bradley et al. 2012; McLure et al. 2013; Bouwens et al. 2015; Finkelstein et al. 2015; Ono et al. 2017; Stefanon et al. 2017) from the literature (see Appendix A and Finkelstein (2016), respectively). The faint, capped error bars and open symbols show the number densities where faint-magnitude incompleteness begins to dominate. The purple curves represent the expected number densities from CLASH after simulating lensing effects on the Bouwens et al. (2015) literature luminosity function. Compared to CLASH, RELICS yields similar number densities of  $z \sim 6$  galaxies, extending to brighter lensed magnitudes ( $H m_{\text{AB}} < 26$ ). At  $z \sim 7$  and  $8$ , RELICS yields somewhat lower number densities.

#### ACKNOWLEDGEMENTS

We thank Gabriel Brammer for insightful discussions related to this work. This paper is based on observations made with the NASA/ESA Hubble Space Telescope. The Space Telescope Science Institute (STScI) is operated by the Association of Universities for Research in Astronomy, Inc. (AURA) under NASA contract NAS 5-26555. ACS was developed under NASA contract NAS 5-32864. The Spitzer Space Telescope is operated by the Jet Propulsion Laboratory, California Institute of Technology under a contract with NASA. These observations are associated with program GO-14096. Archival data are associated with programs GO-9270, GO-12166, GO-12477, GO-12253. Some of the data presented in this paper were obtained from the Mikulski Archive for Space Telescopes (MAST). This work was performed under the auspices of the U.S. Department of Energy by Lawrence Livermore National Laboratory under Contract DE-AC52-07NA27344. F.A.-S. acknowledges support from Chandra grant G03-14131X.

#### REFERENCES

- Alavi, A., Siana, B., Richard, J., et al. 2016, *ApJ*, 832, 56  
 Applegate, D. E., von der Linden, A., Kelly, P. L., et al. 2014, *MNRAS*, 439, 48  
 Atek, H., Richard, J., Kneib, J.-P., et al. 2014, *ApJ*, 786, 60  
 Atek, H., Richard, J., Jauzac, M., et al. 2015a, *ApJ*, 814, 69  
 Atek, H., Richard, J., Kneib, J.-P., et al. 2015b, *ApJ*, 800, 18  
 Beckwith, S. V. W., Stiavelli, M., Koekemoer, A. M., et al. 2006, *AJ*, 132, 1729  
 Benítez, N. 2000, *ApJ*, 536, 571  
 Benítez, N., Ford, H., Bouwens, R., et al. 2004, *ApJS*, 150, 1  
 Bertin, E., & Arnouts, S. 1996, *A&AS*, 117, 393  
 Bleem, L. E., Stalder, B., de Haan, T., et al. 2015, *ApJS*, 216, 27  
 Bouwens, R. J., Illingworth, G. D., Franx, M., & Ford, H. 2007, *ApJ*, 670, 928  
 Bouwens, R. J., Illingworth, G. D., Oesch, P. A., et al. 2017a, *ApJ*, 843, 41  
 Bouwens, R. J., Oesch, P. A., Illingworth, G. D., Ellis, R. S., & Stefanon, M. 2017b, *ApJ*, 843, 129  
 Bouwens, R. J., Illingworth, G. D., Oesch, P. A., et al. 2011, *ApJ*, 737, 90  
 Bouwens, R. J., Bradley, L., Zitrin, A., et al. 2014, *ApJ*, 795, 126  
 Bouwens, R. J., Illingworth, G. D., Oesch, P. A., et al. 2015, *ApJ*, 803, 34  
 Bowler, R. A. A., Dunlop, J. S., McLure, R. J., & McLeod, D. J. 2017, *MNRAS*, 466, 3612  
 Bowler, R. A. A., Dunlop, J. S., McLure, R. J., et al. 2012, *MNRAS*, 426, 2772  
 —. 2014, *MNRAS*, 440, 2810  
 —. 2015, *MNRAS*, 452, 1817  
 Bradley, L. D., Bouwens, R. J., Ford, H. C., et al. 2008, *ApJ*, 678, 647  
 Bradley, L. D., Trenti, M., Oesch, P. A., et al. 2012, *ApJ*, 760, 108  
 Bradley, L. D., Zitrin, A., Coe, D., et al. 2014, *ApJ*, 792, 76

- Brammer, G. B., van Dokkum, P. G., & Coppi, P. 2008, *ApJ*, 686, 1503
- Bullock, J. S., Kolatt, T. S., Sigad, Y., et al. 2001, *MNRAS*, 321, 559
- Bunker, A. J., Stanway, E. R., Ellis, R. S., & McMahon, R. G. 2004, *MNRAS*, 355, 374
- Calvi, V., Trenti, M., Stiavelli, M., et al. 2016, *ApJ*, 817, 120
- Cerny, C., Sheren, K., Coe, D., & et al. 2017, *ApJ* (submitted)
- Coe, D., Benítez, N., Sánchez, S. F., et al. 2006, *AJ*, 132, 926
- Coe, D., Bradley, L., & Zitrin, A. 2015, *ApJ*, 800, 84
- Coe, D., Zitrin, A., Carrasco, M., et al. 2013, *ApJ*, 762, 32
- Cushing, M. C., Rayner, J. T., & Vacca, W. D. 2005, *ApJ*, 623, 1115
- Ebeling, H., Edge, A. C., & Henry, J. P. 2001, *ApJ*, 553, 668
- Ellis, R. S., McLure, R. J., Dunlop, J. S., et al. 2013, *ApJ*, 763, L7
- Erb, D. K., Pettini, M., Shapley, A. E., et al. 2010, *ApJ*, 719, 1168
- Finkelstein, S. L. 2016, *PASA*, 33, e037
- Finkelstein, S. L., Papovich, C., Ryan, R. E., et al. 2012, *ApJ*, 758, 93
- Finkelstein, S. L., Ryan, Jr., R. E., Papovich, C., et al. 2015, *ApJ*, 810, 71
- Fioc, M., & Rocca-Volmerange, B. 1997, *A&A*, 326, 950
- Franx, M., Illingworth, G. D., Kelson, D. D., van Dokkum, P. G., & Tran, K.-V. 1997, *ApJ*, 486, L75
- Gonzaga, S., & et al. 2012, *The DrizzlePac Handbook*
- Grogin, N. A., Kocevski, D. D., Faber, S. M., et al. 2011, *ApJS*, 197, 35
- Harikane, Y., Ouchi, M., Ono, Y., et al. 2017, *ArXiv e-prints*, arXiv:1704.06535
- Hasselfield, M., Hilton, M., Marriage, T. A., et al. 2013, *J. Cosmology Astropart. Phys.*, 7, 008
- Hoag, A., Bradač, M., Trenti, M., et al. 2017, *Nature Astronomy*, 1, 0091
- Hoekstra, H., Herbonnet, R., Muzzin, A., et al. 2015, *MNRAS*, 449, 685
- Illingworth, G. D., Magee, D., Oesch, P. A., et al. 2013, *ApJS*, 209, 6
- Ishigaki, M., Kawamata, R., Ouchi, M., Oguri, M., & Shimasaku, K. 2017, *ArXiv e-prints*, arXiv:1702.04867
- Ishigaki, M., Kawamata, R., Ouchi, M., et al. 2015, *ApJ*, 799, 12
- Jones, T. A., Ellis, R. S., Schenker, M. A., & Stark, D. P. 2013, *ApJ*, 779, 52
- Kawamata, R., Ishigaki, M., Shimasaku, K., Oguri, M., & Ouchi, M. 2015, *ApJ*, 804, 103
- Koekemoer, A. M., Faber, S. M., Ferguson, H. C., et al. 2011, *ApJS*, 197, 36
- Koekemoer, A. M., Ellis, R. S., McLure, R. J., et al. 2013, *ApJS*, 209, 3
- Konno, A., Ouchi, M., Shibuya, T., et al. 2017, *ArXiv e-prints*, arXiv:1705.01222
- Kuhlen, M., & Faucher-Giguère, C.-A. 2012, *MNRAS*, 423, 862
- Livermore, R. C., Finkelstein, S. L., & Lotz, J. M. 2017, *ApJ*, 835, 113
- Lotz, J. M., Koekemoer, A., Coe, D., et al. 2017, *ApJ*, 837, 97
- Madau, P. 1995, *ApJ*, 441, 18
- Madau, P., Haardt, F., & Rees, M. J. 1999, *ApJ*, 514, 648
- Mainali, R., Kollmeier, J. A., Stark, D. P., et al. 2017, *ApJ*, 836, L14
- Mantz, A., Allen, S. W., Ebeling, H., Rapetti, D., & Drlica-Wagner, A. 2010, *MNRAS*, 406, 1773
- Maraston, C. 2005, *MNRAS*, 362, 799
- McCracken, H. J., Milvang-Jensen, B., Dunlop, J., et al. 2012, *A&A*, 544, A156
- McLeod, D. J., McLure, R. J., & Dunlop, J. S. 2016, *MNRAS*, 459, 3812
- McLure, R. J., Dunlop, J. S., Bowler, R. A. A., et al. 2013, *MNRAS*, 432, 2696
- Meneghetti, M., Natarajan, P., Coe, D., et al. 2017, *MNRAS*, 472, 3177
- Merlin, E., Bourne, N., Castellano, M., et al. 2016, *A&A*, 595, A97
- Neto, A. F., Gao, L., Bett, P., et al. 2007, *MNRAS*, 381, 1450
- Oesch, P. A., Bouwens, R. J., Illingworth, G. D., et al. 2015, *ApJ*, 808, 104
- Oesch, P. A., Carollo, C. M., Stiavelli, M., et al. 2009, *ApJ*, 690, 1350
- Oesch, P. A., Bouwens, R. J., Illingworth, G. D., et al. 2012, *ApJ*, 759, 135
- Oesch, P. A., Brammer, G., van Dokkum, P. G., et al. 2016, *ApJ*, 819, 129
- Oke, J. B., & Gunn, J. E. 1983, *ApJ*, 266, 713
- Ono, Y., Ouchi, M., Harikane, Y., et al. 2017, *ArXiv e-prints*, arXiv:1704.06004
- Ouchi, M., Harikane, Y., Shibuya, T., et al. 2017, *ArXiv e-prints*, arXiv:1704.07455
- Pentericci, L., Vanzella, E., Fontana, A., et al. 2014, *ApJ*, 793, 113
- Piffaretti, R., Arnaud, M., Pratt, G. W., Pointecouteau, E., & Melin, J.-B. 2011, *A&A*, 534, A109
- Planck Collaboration, Ade, P. A. R., Aghanim, N., et al. 2016, *A&A*, 594, A27
- Postman, M., Coe, D., Benítez, N., et al. 2012, *ApJS*, 199, 25
- Rayner, J. T., Cushing, M. C., & Vacca, W. D. 2009, *ApJS*, 185, 289
- Rigby, J. R., Bayliss, M. B., Gladders, M. D., et al. 2015, *ApJ*, 814, L6
- Robertson, B. E., Ellis, R. S., Furlanetto, S. R., & Dunlop, J. S. 2015, *ApJ*, 802, L19
- Schechter, P. 1976, *ApJ*, 203, 297
- Schenker, M. A., Stark, D. P., Ellis, R. S., et al. 2012, *ApJ*, 744, 179
- Schlafly, E. F., & Finkbeiner, D. P. 2011, *ApJ*, 737, 103
- Schmidt, K. B., Treu, T., Trenti, M., et al. 2014, *ApJ*, 786, 57
- Scoville, N., Aussel, H., Brusa, M., et al. 2007, *ApJS*, 172, 1
- Sereno, M. 2015, *MNRAS*, 450, 3665
- Shibuya, T., Ouchi, M., Konno, A., et al. 2017a, *ArXiv e-prints*, arXiv:1704.08140
- Shibuya, T., Ouchi, M., Harikane, Y., et al. 2017b, *ArXiv e-prints*, arXiv:1705.00733
- Stark, D. P. 2016, *ARA&A*, 54, 761
- Stark, D. P., Ellis, R. S., Chiu, K., Ouchi, M., & Bunker, A. 2010, *MNRAS*, 408, 1628
- Stark, D. P., Richard, J., Siana, B., et al. 2014, *MNRAS*, 445, 3200
- Stark, D. P., Walth, G., Charlot, S., et al. 2015a, *MNRAS*, 454, 1393
- Stark, D. P., Richard, J., Charlot, S., et al. 2015b, *MNRAS*, 450, 1846
- Stark, D. P., Ellis, R. S., Charlot, S., et al. 2017, *MNRAS*, 464, 469
- Stefanon, M., Labbé, I., Bouwens, R. J., et al. 2017, *ArXiv e-prints*, arXiv:1706.04613
- Tilvi, V., Papovich, C., Tran, K.-V. H., et al. 2013, *ApJ*, 768, 56
- Trenti, M., Bradley, L. D., Stiavelli, M., et al. 2011, *ApJ*, 727, L39
- Umetsu, K., Medezinski, E., Nonino, M., et al. 2014, *ApJ*, 795, 163
- Vanzella, E., De Barros, S., Cupani, G., et al. 2016, *ApJ*, 821, L27
- Vanzella, E., Calura, F., Meneghetti, M., et al. 2017, *MNRAS*, 467, 4304
- von der Linden, A., Allen, M. T., Applegate, D. E., et al. 2014, *MNRAS*, 439, 2
- Wen, Z. L., Han, J. L., & Liu, F. S. 2012, *ApJS*, 199, 34
- Wong, K. C., Zabludoff, A. I., Ammons, S. M., et al. 2013, *ApJ*, 769, 52
- Wright, E. L., Eisenhardt, P. R. M., Mainzer, A. K., et al. 2010, *AJ*, 140, 1868
- Yan, H., Windhorst, R. A., & Cohen, S. H. 2003, *ApJ*, 585, L93
- Zheng, W., Postman, M., Zitrin, A., et al. 2012, *Nature*, 489, 406
- Zitrin, A., Moustakas, J., Bradley, L., et al. 2012, *ApJ*, 747, L9
- Zitrin, A., Zheng, W., Broadhurst, T., et al. 2014, *ApJ*, 793, L12

## APPENDIX

## THE BRIGHT END OF THE UV LUMINOSITY FUNCTION

The regions on the sky immediately surrounding RELICS clusters will benefit from substantial amounts of lensing magnification and therefore should benefit from a significant enhancement in the surface density of especially bright, highly magnified sources. While one would expect more bright sources in lensing fields relative to Schechter representations of the  $UV$  LF at  $z \sim 6-8$ , we must take notice that the consensus of the un-lensed bright end  $UV$  LF has changed in recent years. Thanks to recent wide-field surveys, there is now increasingly compelling evidence that the bright end of the  $z \sim 6-8$   $UV$  LF exhibits more of a double power-law form (Bowler et al. 2014, 2015; Ono et al. 2017):

$$\phi^* \left[ \left( \frac{L}{L^*} \right)^{-\alpha} + \left( \frac{L}{L^*} \right)^{-\gamma} \right]^{-1} \frac{dL}{L^*} \quad (\text{A1})$$

Compared to a relatively abrupt bright-end cut-off inherent to Schechter function fits, the double power-law form of the LF accurately recovers the larger number of observed bright sources and plausibly yields a similar number of bright sources to what we would expect based on lensing magnification from our RELICS sample.

Therefore, to demonstrate more clearly the gains one achieves in identifying bright sources behind lensing clusters (vs. blank field searches), we make use of double power-law representations of the LF results in the literature. In deriving these double power-law LF results, we make use of LF constraints from the Hubble Ultra Deep Field, the Hubble Ultra Deep Field parallel fields, Hubble Frontier Field parallel fields, CANDELS, UltraVISTA, UDS, and the Hyper-Suprime-Cam fields. We executed these fits using a Markov-chain Monte-Carlo procedure.

At  $z \sim 6$ , we make use of the published stepwise LF constraints from Bouwens et al. (2007, 2015); Finkelstein et al. (2015); Bowler et al. (2015); Ono et al. (2017); at  $z \sim 7$ , we make use of LF constraints from McLure et al. (2013); Bouwens et al. (2015); Finkelstein et al. (2015); Bowler et al. (2017); Ono et al. (2017); at  $z \sim 8$ , we make use of LF constraints from Oesch et al. (2012); Bradley et al. (2012); McLure et al. (2013); Bouwens et al. (2015); Finkelstein et al. (2015); Stefanon et al. (2017).

For LF constraints derived from Lyman-break selections, where the mean redshift is less than that for photometric redshift selections, we have adjusted the published volume densities to the expected differences relative to the LF results at  $z = 6$ ,  $z = 7$ , and  $z = 8$ . Specifically, we adjusted the Bouwens et al. (2015)  $z = 5.9$ ,  $z = 6.8$ , and  $z = 7.9$  downwards by 0.02 dex, 0.04 dex, and 0.02 dex, respectively, and Bouwens et al. (2007)  $z = 5.9$  results downwards by 0.02 dex.

A few points in the aforementioned LF determinations from the literature appear to be subject to sizable systematics, and are therefore excluded from our LF fits. Among these is the faintest stepwise point in the  $z \sim 7$  LF from Bowler et al. (2017) which is discrepant by several sigma from the other LF determinations. It is likely that this point is impacted by uncertainties in the estimated completeness at the faint end of UltraVISTA, and not due to the start of a shallower faint-end slope. Also excluded are the intermediate-luminosity (i.e.,  $-20$  to  $-19$ )  $z \sim 6$  and  $z \sim 7$  stepwise points from Finkelstein et al. (2015), which receive a dominant contribution from search results over CANDELS. These points were excluded because the faint-end corrections for completeness over the CANDELS fields may have been overestimated, which accounts for the differences between the results by Finkelstein et al. (2015) and the results from other fields, such as Bouwens et al. (2015) and McLure et al. (2013).

The best-fit double-law LF results we obtain are presented in Figure 15 with the red solid lines. The best-fit double power-law parameters are  $\phi^* = 0.000175 \text{ Mpc}^{-3}$ ,  $M^* = -21.22$ ,  $\alpha = -2.08$ ,  $\gamma = -4.78$  at  $z \sim 6$ ,  $\phi^* = 0.000204 \text{ Mpc}^{-3}$ ,  $M^* = -20.70$ ,  $\alpha = -2.15$ ,  $\gamma = -4.37$  at  $z \sim 7$ ,  $\phi^* = 0.000538 \text{ Mpc}^{-3}$ ,  $M^* = -19.71$ ,  $\alpha = -1.91$ ,  $\gamma = -3.61$  at  $z \sim 8$ . As the present results also represent fits to LF results in the literature, our fit results are in reasonable agreement with previous literature-averaged fits by Finkelstein (2016) using a Schechter functional form at all luminosities except the extreme bright end.

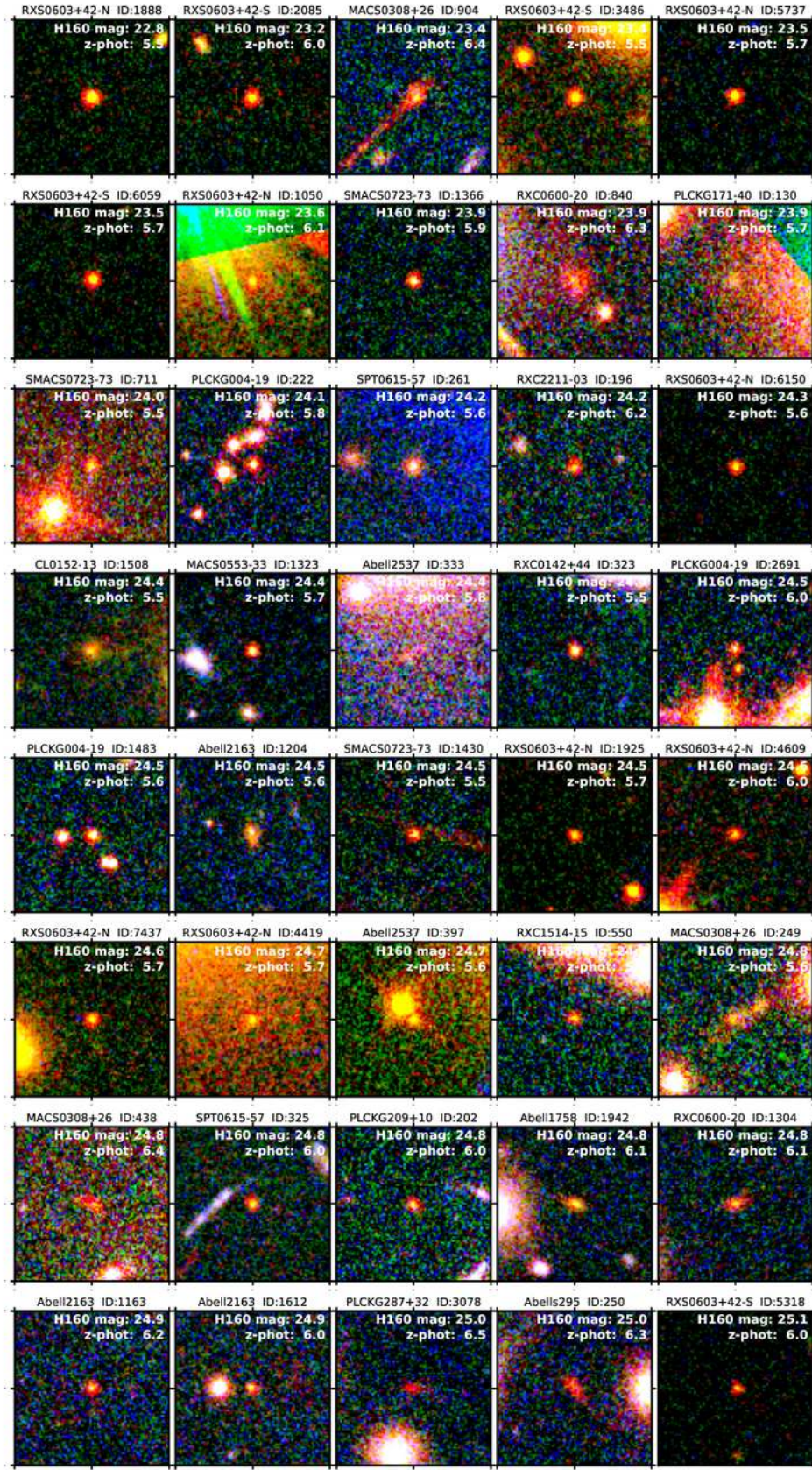


**Figure 8.** The brightest 40 galaxy candidates from the  $z \sim 6$  RELICS sample. Each RGB color image stamp is  $5'' \times 5''$  with the red channel as the sum of all IR bands, the G channel as the ACS F814W band, and the B channel the sum of ACS F435W and F606W. The F160W  $H$ -band AB magnitude is shown within each stamp, along with the adopted redshift (see § 2.4). The cluster name and catalog ID are shown at the top of each stamp.

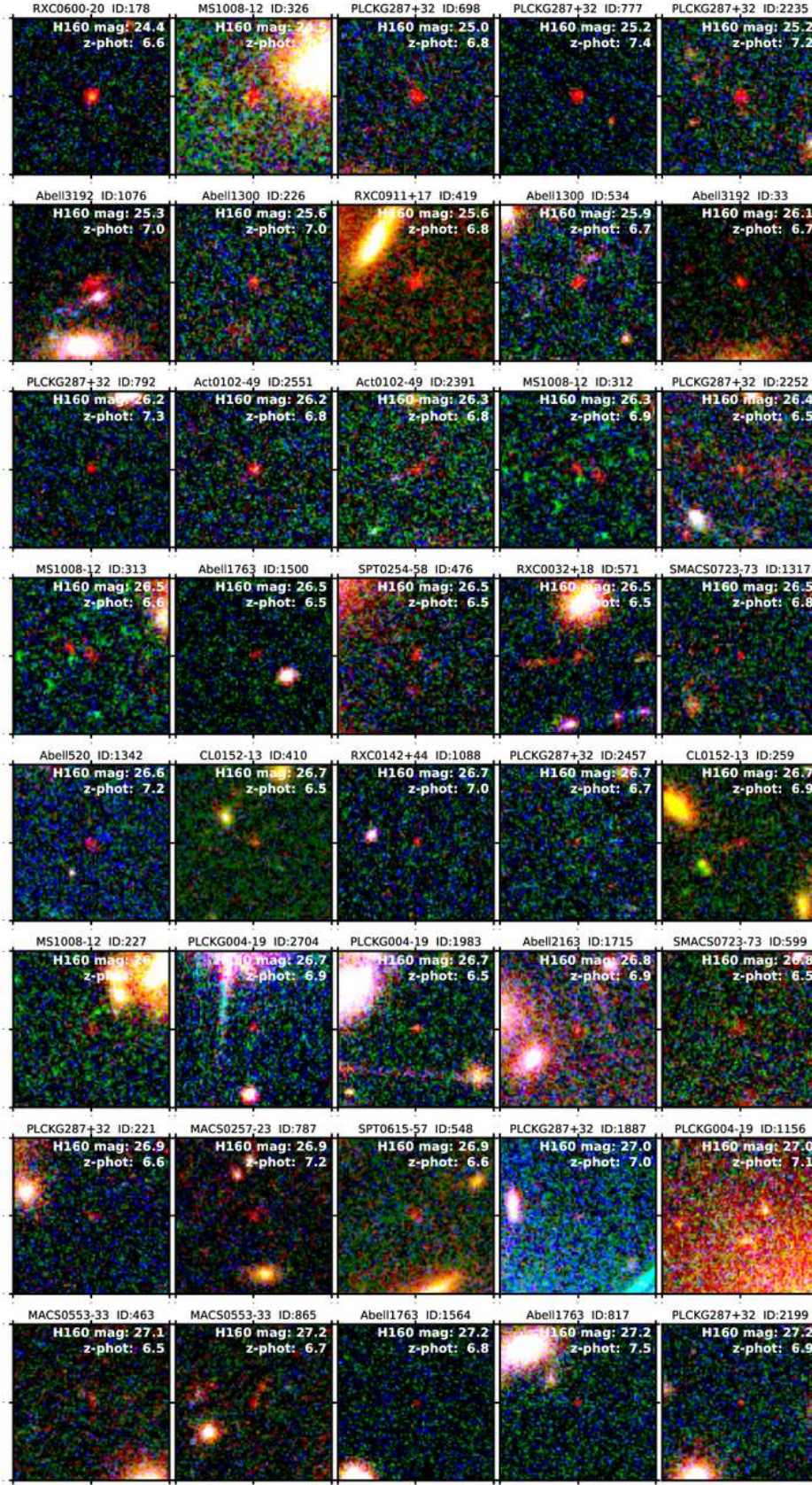
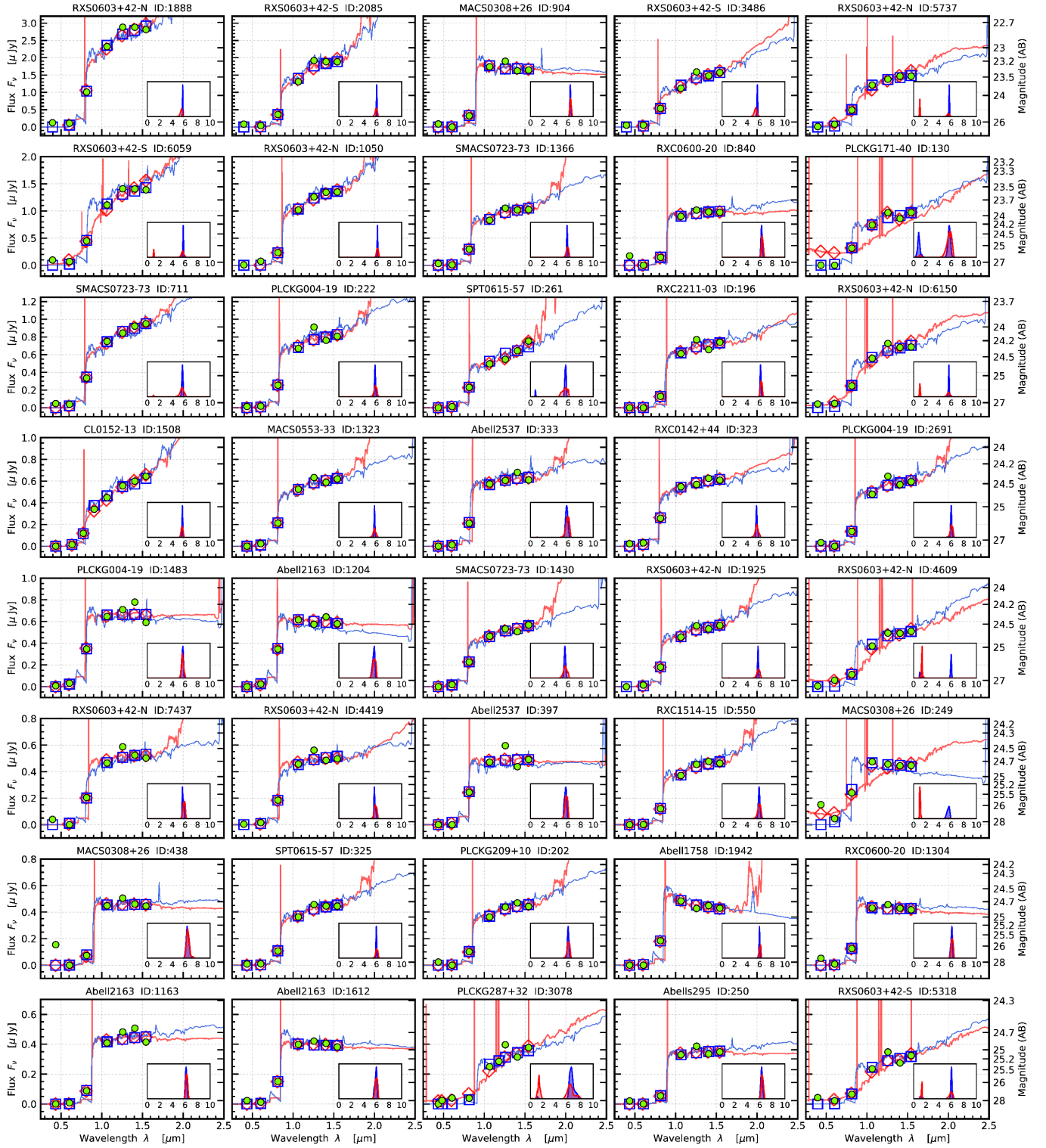
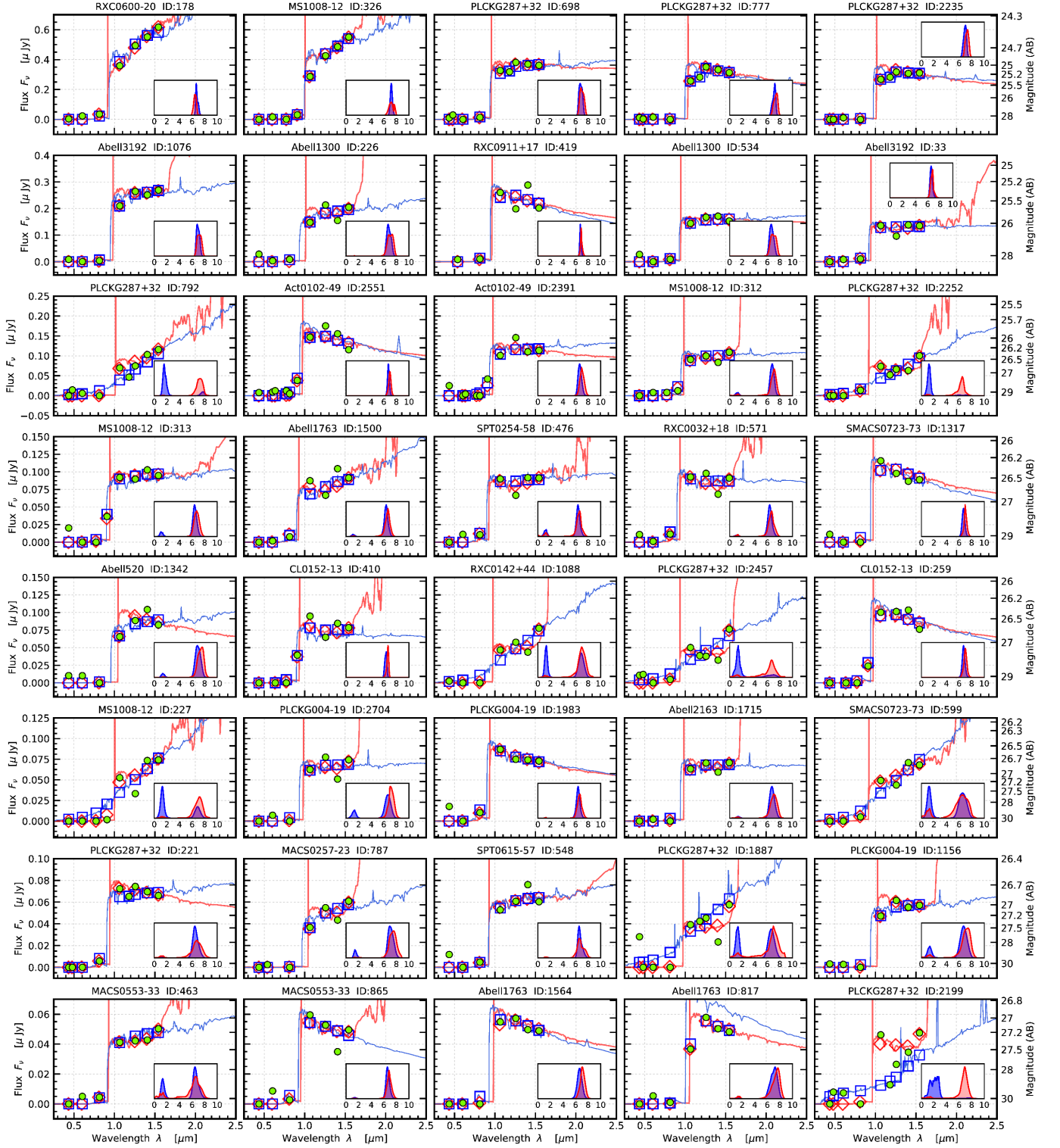


Figure 9. The same as Fig. 8 but for the brightest 40 objects from the  $z \sim 7$  sample.



**Figure 10.** The best-fit SEDs from EAZY (red) and BPZ (blue) for the 40 brightest galaxy candidates from the  $z \sim 6$  RELICS sample. The diamonds and squares show the expected fluxes from the model SED for EAZY and BPZ respectively, and the green circles are the RELICS data. The typical photometric uncertainties are about the size of the data points. The top title shows the cluster and catalog ID number of each high- $z$  candidate. The grid of this plot matches to the galaxies shown in Fig. 8.



**Figure 11.** The same as Fig. 10 but showing the 40 brightest galaxies from the  $z \sim 7$  RELICS sample. The grid of this plot matches to the galaxies shown in Fig. 9.

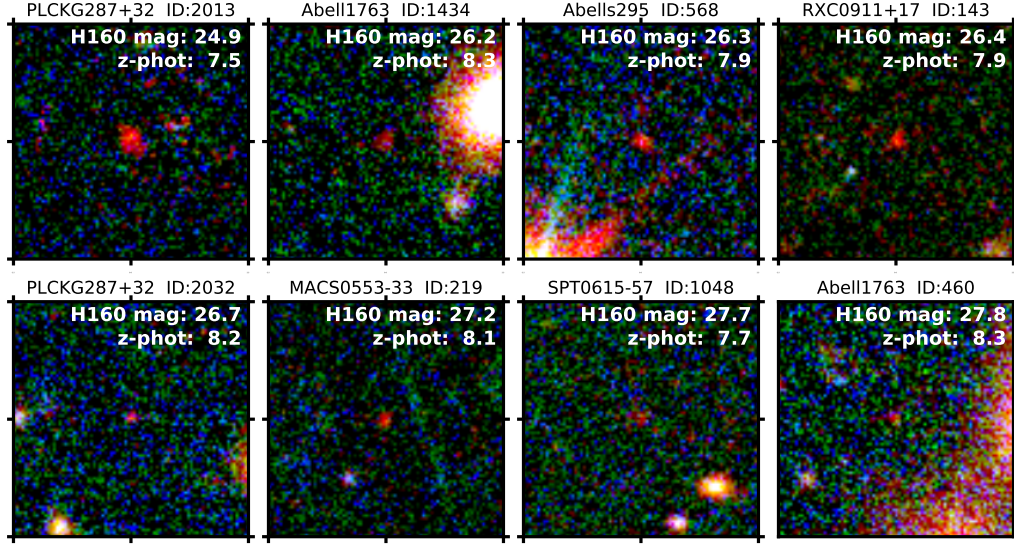


**Figure 12.** All galaxy candidates from the  $z \sim 8$  RELICS sample. Each RGB color image stamp is  $5'' \times 5''$  with the red channel as the sum of all IR bands, the G channel as the ACS F814W band, and the B channel the sum of ACS F435W and F606W. The F160W  $H$ -band AB magnitude is shown within each stamp, along with the adopted redshift (see § 2.4). The cluster name and catalog ID are shown at the top of each stamp.

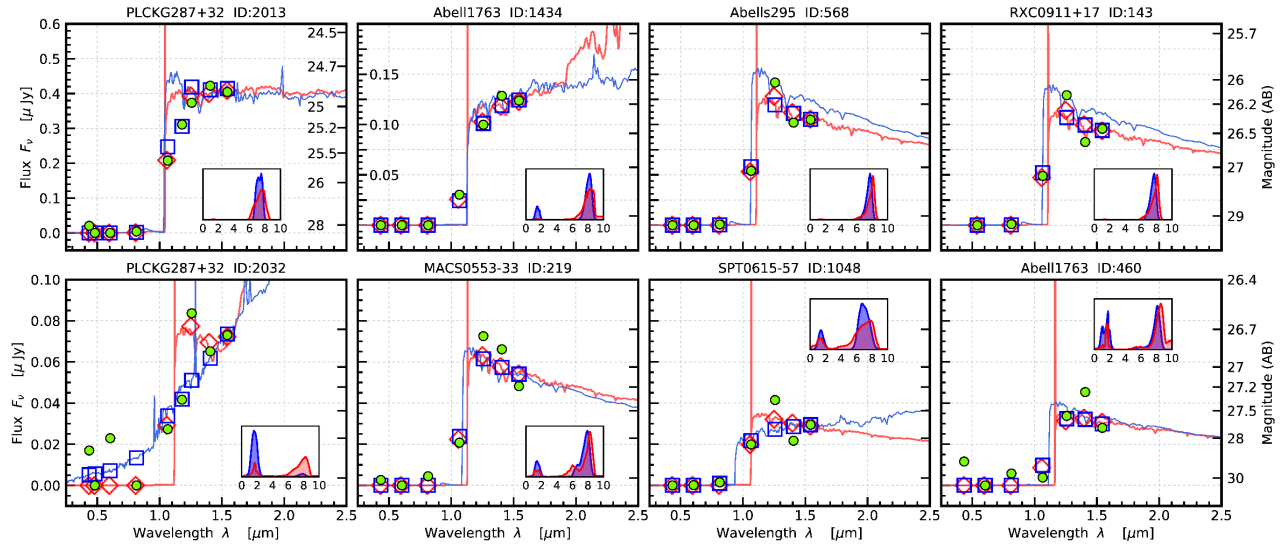


**Figure 13.** The best-fit SEDs from EAZY (red) and BPZ (blue) for all galaxy candidates from the  $z \sim 8$  RELICS sample. The diamonds and squares show the expected fluxes from the model SED for EAZY and BPZ respectively, and the green circles are the RELICS data. The typical photometric uncertainties are about the size of the data points. The top title shows the cluster and catalog ID number of each high- $z$  candidate. The grid of this plot matches to the galaxies shown in Fig. 12.



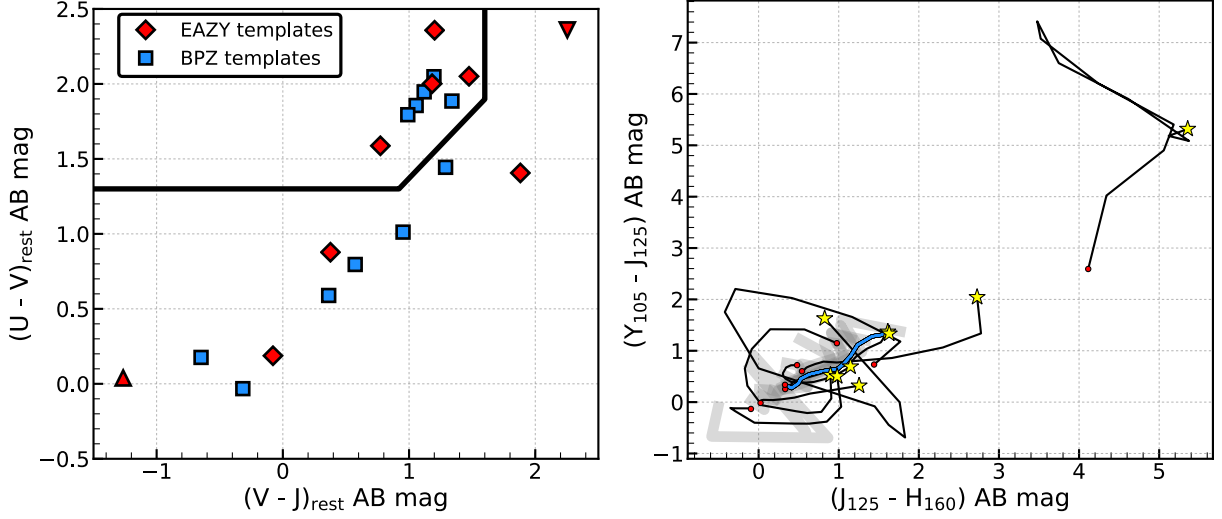


**Figure 14.** Left: Rest-frame UVJ colors of the default SED templates used by EAZY (red diamonds) and BPZ (blue squares). The downward triangle is a very dusty SED template and the upward triangle is an extreme nebular emission line template from EAZY. While both codes use linear combinations of these templates to span a wide range of colors, the different assumed templates are the primary source for any photometric-redshift disagreement. Right: WFC3 YJH colors for the nine default EAZY SED templates. The gray thick lines follow the colors of each template with increasing redshift from  $z = 0.5$  to the red circle at  $z = 2$ . The black line continues to show the colors with increasing redshift until the yellow star at  $z = 11$ . The blue line shows the extreme nebular emission line template, which has very degenerate colors at  $z > 5$  with those at  $z < 3$ . The convergence of the  $z = 10$ – $11$  yellow stars emphasizes the difficulty in distinguishing between galaxies at  $z < 2$  and  $z > 9$ .

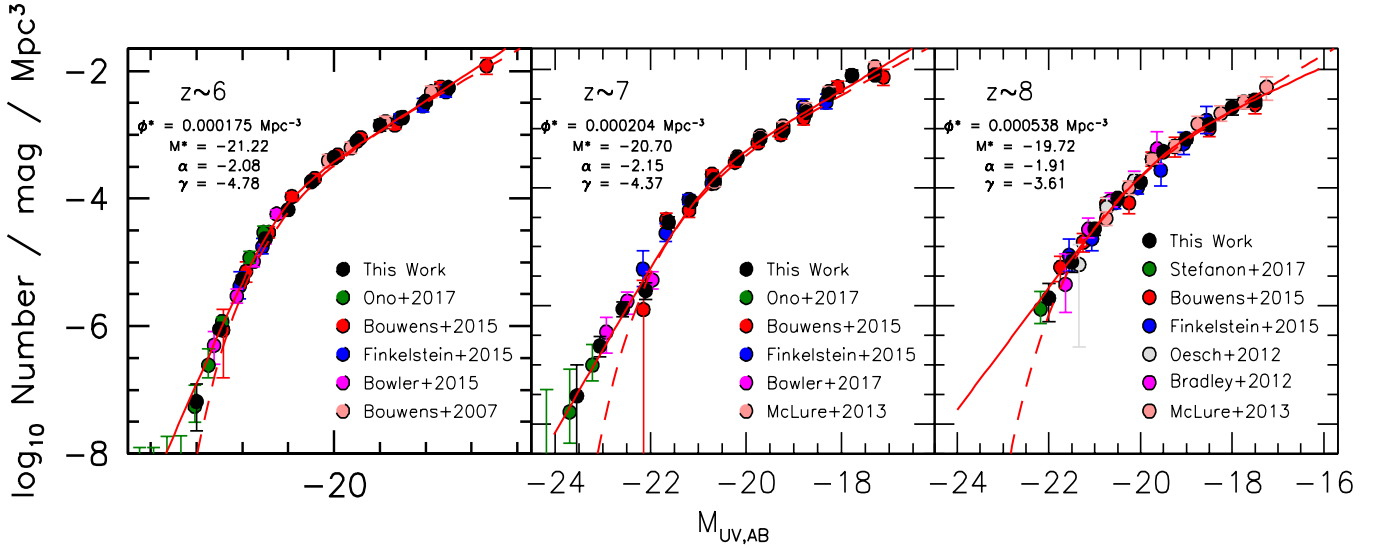


**Figure 15.** Best-fit double power-law determinations of the  $z \sim 6$ ,  $z \sim 7$ , and  $z \sim 8$  LF results using a comprehensive set of published LF results from the literature (solid circles). Best-fit LF parameters are included in each panel, while the solid red lines show the double-power law fits. Included in the  $z \sim 6$  fits are the determinations from Bouwens et al. (2007, 2015); Finkelstein et al. (2015); Bowler et al. (2015); Ono et al. (2017); included in the  $z \sim 7$  fits are determinations from McLure et al. (2013); Bouwens et al. (2015); Finkelstein et al. (2015); Bowler et al. (2017); Ono et al. (2017); included in the  $z \sim 8$  fits are determinations from Oesch et al. (2012); Bradley et al. (2012); McLure et al. (2013); Bouwens et al. (2015); Finkelstein et al. (2015); Stefanon et al. (2017). Slight adjustments (10–20%) have been made to the volume density of individual points to account for slight differences in the mean redshifts of the derived LF results. The faintest constraint on the  $z \sim 7$  LF from Bowler et al. (2015) and several intermediate luminosity LF constraints from Finkelstein et al. (2015) due to concerns they likely overestimate the completeness of the UltraVISTA and CANDELS selections. The Finkelstein (2016) literature-averaged Schechter fits are shown with the dashed lines.

**Table 2**  
 $z \sim 6$  Galaxy Candidates Behind 41 RELICS Clusters

| Object ID <sup>a</sup> | $\alpha_{J2000}$ | $\delta_{J2000}$ | $B_{435}$  | $V_{606}$  | $I_{814}$  | $Y_{105}$  | $J_{125}$  | $JH_{140}$ | $H_{160}$  | $z_{EZ}^b$                          | $z_{BPZ}^c$                         |
|------------------------|------------------|------------------|------------|------------|------------|------------|------------|------------|------------|-------------------------------------|-------------------------------------|
| RXS0603+42-N-1888      | 90.793252        | 42.270382        | ...        | 26.31±0.18 | 23.89±0.01 | 22.99±0.02 | 22.75±0.02 | 22.75±0.02 | 22.78±0.01 | 5.4 <sup>+0.2</sup> <sub>-0.4</sub> | 5.6 <sup>+0.1</sup> <sub>-0.1</sub> |
| RXS0603+42-S-2085      | 90.864338        | 42.182232        | ...        | 27.38±0.36 | 25.01±0.03 | 23.61±0.03 | 23.19±0.04 | 23.21±0.03 | 23.21±0.02 | 5.9 <sup>+0.3</sup> <sub>-0.3</sub> | 6.0 <sup>+0.1</sup> <sub>-0.1</sub> |
| MACS0308+26-0904       | 47.222529        | 26.749704        | 26.54±0.49 | > 27.8     | 25.12±0.12 | 23.30±0.03 | 23.20±0.05 | 23.37±0.04 | 23.36±0.03 | 6.4 <sup>+0.2</sup> <sub>-0.2</sub> | 6.3 <sup>+0.1</sup> <sub>-0.1</sub> |
| RXS0603+42-S-3486      | 90.853690        | 42.171170        | ...        | 27.10±0.30 | 24.58±0.02 | 23.78±0.03 | 23.40±0.03 | 23.47±0.03 | 23.41±0.02 | 5.4 <sup>+0.3</sup> <sub>-0.5</sub> | 5.6 <sup>+0.1</sup> <sub>-0.1</sub> |
| RXS0603+42-N-5737      | 90.788352        | 42.248042        | ...        | 26.65±0.21 | 24.67±0.02 | 23.69±0.03 | 23.55±0.04 | 23.48±0.03 | 23.48±0.02 | 1.0 <sup>+4.8</sup> <sub>-0.1</sub> | 5.7 <sup>+0.1</sup> <sub>-0.1</sub> |
| RXS0603+42-S-6059      | 90.863787        | 42.150244        | ...        | 26.79±0.25 | 24.77±0.03 | 23.79±0.03 | 23.53±0.04 | 23.53±0.03 | 23.54±0.02 | 1.0 <sup>+4.9</sup> <sub>-0.1</sub> | 5.7 <sup>+0.1</sup> <sub>-0.1</sub> |
| RXS0603+42-N-1050      | 90.786687        | 42.276517        | ...        | 26.72±0.39 | 25.49±0.05 | 23.88±0.03 | 23.65±0.04 | 23.58±0.04 | 23.57±0.02 | 6.1 <sup>+0.3</sup> <sub>-0.2</sub> | 6.1 <sup>+0.1</sup> <sub>-0.1</sub> |
| SMACS0723-73-1366      | 110.813866       | -73.469150       | 27.68±0.67 | 29.08±1.02 | 25.22±0.07 | 24.10±0.03 | 23.85±0.04 | 23.88±0.04 | 23.87±0.03 | 5.9 <sup>+0.3</sup> <sub>-0.3</sub> | 5.8 <sup>+0.1</sup> <sub>-0.1</sub> |
| RXC0600-20-0840        | 90.039804        | -20.136336       | 25.80±0.22 | > 28.2     | 25.99±0.16 | 24.01±0.04 | 23.88±0.07 | 23.92±0.06 | 23.93±0.04 | 6.4 <sup>+0.3</sup> <sub>-0.2</sub> | 6.3 <sup>+0.2</sup> <sub>-0.2</sub> |
| PLCKG171-40-0130       | 48.225851        | 8.384411         | > 25.9     | > 26.8     | 25.15±0.20 | 24.22±0.10 | 23.93±0.12 | 24.07±0.11 | 23.93±0.06 | 5.8 <sup>+0.4</sup> <sub>-1.1</sub> | 5.7 <sup>+0.3</sup> <sub>-5.1</sub> |
| SMACS0723-73-0711      | 110.810518       | -73.452826       | 27.22±0.59 | 27.42±0.39 | 25.09±0.07 | 24.21±0.04 | 24.08±0.06 | 23.99±0.05 | 23.96±0.03 | 5.5 <sup>+0.5</sup> <sub>-0.2</sub> | 5.6 <sup>+0.1</sup> <sub>-0.2</sub> |
| PLCKG004-19-0222       | 289.282178       | -33.508191       | 28.51±0.87 | 28.28±0.56 | 25.38±0.07 | 24.33±0.06 | 24.00±0.07 | 24.20±0.07 | 24.13±0.05 | 5.8 <sup>+0.3</sup> <sub>-0.4</sub> | 5.8 <sup>+0.1</sup> <sub>-0.1</sub> |
| SPT0615-57-0261        | 93.955568        | -57.770519       | > 28.2     | 28.64±0.67 | 25.50±0.05 | 24.66±0.05 | 24.56±0.08 | 24.38±0.06 | 24.21±0.04 | 5.7 <sup>+0.4</sup> <sub>-0.9</sub> | 5.6 <sup>+0.1</sup> <sub>-4.8</sub> |
| RXC2211-03-0196        | 332.945088       | -3.816933        | > 28.2     | > 28.9     | 26.13±0.13 | 24.43±0.04 | 24.18±0.06 | 24.36±0.06 | 24.23±0.03 | 6.2 <sup>+0.3</sup> <sub>-0.2</sub> | 6.1 <sup>+0.1</sup> <sub>-0.1</sub> |
| RXS0603+42-N-6150      | 90.790722        | 42.245871        | ...        | 27.17±0.29 | 25.42±0.04 | 24.53±0.04 | 24.25±0.06 | 24.32±0.05 | 24.31±0.03 | 1.0 <sup>+4.9</sup> <sub>-0.1</sub> | 5.6 <sup>+0.1</sup> <sub>-0.1</sub> |
| CL0152-13-1508         | 28.165607        | -13.968644       | > 28.1     | ...        | ...        | 24.77±0.07 | 24.54±0.04 | 24.46±0.08 | 24.38±0.03 | 5.5 <sup>+0.3</sup> <sub>-0.2</sub> | 5.6 <sup>+0.1</sup> <sub>-0.1</sub> |
| MACS0553-33-1323       | 88.355157        | -33.726948       | > 29.1     | 27.98±0.32 | 25.58±0.04 | 24.60±0.05 | 24.40±0.06 | 24.48±0.06 | 24.42±0.04 | 5.7 <sup>+0.4</sup> <sub>-0.4</sub> | 5.7 <sup>+0.1</sup> <sub>-0.1</sub> |
| RXC0142+44-0323        | 25.752926        | 44.642511        | 28.02±0.58 | 27.70±0.32 | 25.37±0.06 | 24.55±0.04 | 24.51±0.07 | 24.41±0.05 | 24.44±0.04 | 5.5 <sup>+0.4</sup> <sub>-0.5</sub> | 5.5 <sup>+0.3</sup> <sub>-0.1</sub> |
| Abell2537-0333         | 347.104166       | -2.188587        | > 27.4     | 28.76±1.24 | 25.59±0.16 | 24.50±0.08 | 24.44±0.14 | 24.32±0.11 | 24.44±0.08 | 5.8 <sup>+0.4</sup> <sub>-0.5</sub> | 5.8 <sup>+0.3</sup> <sub>-0.3</sub> |
| PLCKG004-19-2691       | 289.265221       | -33.544507       | 27.60±0.44 | > 0.0      | 26.06±0.11 | 24.70±0.08 | 24.38±0.09 | 24.52±0.09 | 24.47±0.05 | 6.0 <sup>+0.4</sup> <sub>-0.4</sub> | 6.0 <sup>+0.1</sup> <sub>-0.2</sub> |
| PLCKG004-19-1483       | 289.287163       | -33.524637       | 29.15±1.31 | 27.64±0.35 | 25.05±0.05 | 24.37±0.04 | 24.27±0.06 | 24.17±0.05 | 24.47±0.05 | 5.5 <sup>+0.4</sup> <sub>-0.2</sub> | 5.7 <sup>+0.1</sup> <sub>-0.3</sub> |
| Abell2163-1204         | 243.918954       | -6.147594        | > 27.3     | 27.97±0.72 | 25.05±0.06 | 24.43±0.06 | 24.50±0.10 | 24.38±0.08 | 24.49±0.05 | 5.6 <sup>+0.4</sup> <sub>-0.4</sub> | 5.6 <sup>+0.1</sup> <sub>-0.4</sub> |
| SMACS0723-73-1430      | 110.859546       | -73.472110       | > 27.9     | 28.21±0.57 | 25.51±0.09 | 24.73±0.05 | 24.58±0.08 | 24.64±0.07 | 24.51±0.04 | 5.5 <sup>+0.5</sup> <sub>-0.6</sub> | 5.5 <sup>+0.2</sup> <sub>-0.2</sub> |
| RXS0603+42-N-1925      | 90.824322        | 42.270199        | ...        | 28.51±0.75 | 25.76±0.06 | 24.75±0.05 | 24.53±0.07 | 24.59±0.06 | 24.52±0.04 | 5.7 <sup>+0.4</sup> <sub>-0.4</sub> | 5.7 <sup>+0.1</sup> <sub>-0.1</sub> |
| RXS0603+42-N-4609      | 90.786605        | 42.253922        | ...        | 26.97±0.22 | 26.28±0.08 | 24.97±0.06 | 24.67±0.07 | 24.67±0.07 | 24.63±0.04 | 1.4 <sup>+0.1</sup> <sub>-0.2</sub> | 6.0 <sup>+0.1</sup> <sub>-5.0</sub> |
| RXS0603+42-N-7437      | 90.810315        | 42.239204        | ...        | > 28.7     | 25.62±0.04 | 24.73±0.04 | 24.48±0.06 | 24.60±0.05 | 24.65±0.04 | 5.9 <sup>+0.2</sup> <sub>-0.3</sub> | 5.6 <sup>+0.3</sup> <sub>-0.1</sub> |
| RXS0603+42-N-4419      | 90.775132        | 42.255014        | ...        | 28.44±0.57 | 25.73±0.04 | 24.75±0.06 | 24.53±0.09 | 24.68±0.08 | 24.66±0.05 | 5.8 <sup>+0.4</sup> <sub>-0.4</sub> | 5.6 <sup>+0.1</sup> <sub>-0.1</sub> |
| Abell2537-0397         | 347.105646       | -2.188369        | > 28.4     | > 0.0      | 25.43±0.06 | 24.72±0.04 | 24.46±0.06 | 24.80±0.07 | 24.67±0.04 | 5.7 <sup>+0.4</sup> <sub>-0.3</sub> | 5.6 <sup>+0.2</sup> <sub>-0.3</sub> |
| RXC1514-15-0550        | 228.758541       | -15.382887       | > 28.1     | 31.41±2.78 | 26.20±0.15 | 24.98±0.07 | 24.76±0.09 | 24.70±0.07 | 24.74±0.05 | 5.9 <sup>+0.4</sup> <sub>-0.3</sub> | 5.9 <sup>+0.2</sup> <sub>-0.2</sub> |
| SPT0615-57-0325        | 93.978235        | -57.771646       | 29.09±1.00 | 28.94±0.65 | 26.33±0.06 | 25.00±0.06 | 24.75±0.07 | 24.78±0.06 | 24.78±0.04 | 6.0 <sup>+0.3</sup> <sub>-0.3</sub> | 6.0 <sup>+0.1</sup> <sub>-0.1</sub> |
| MACS0308+26-0438       | 47.238287        | 26.763436        | 25.93±0.22 | > 28.4     | 26.75±0.33 | 24.77±0.06 | 24.64±0.09 | 24.74±0.08 | 24.78±0.06 | 6.4 <sup>+0.5</sup> <sub>-0.3</sub> | 6.3 <sup>+0.5</sup> <sub>-0.3</sub> |
| MACS0308+26-0249       | 47.237605        | 26.768654        | 25.95±0.24 | 27.25±0.36 | 25.45±0.12 | 24.71±0.07 | 24.75±0.11 | 24.78±0.09 | 24.78±0.06 | 1.0 <sup>+0.3</sup> <sub>-0.1</sub> | 5.6 <sup>+0.2</sup> <sub>-0.5</sub> |
| PLCKG209+10-0202       | 110.587210       | 7.420105         | 27.96±0.59 | > 28.9     | 26.39±0.17 | 25.00±0.06 | 24.80±0.09 | 24.72±0.07 | 24.79±0.05 | 6.0 <sup>+0.4</sup> <sub>-0.4</sub> | 6.0 <sup>+0.2</sup> <sub>-0.2</sub> |
| Abell1758-1942         | 203.200110       | 50.518517        | > 28.7     | > 29.1     | 25.74±0.05 | 24.69±0.05 | 24.82±0.09 | 24.77±0.07 | 24.82±0.05 | 6.2 <sup>+0.1</sup> <sub>-0.4</sub> | 6.0 <sup>+0.1</sup> <sub>-0.2</sub> |
| RXC0600-20-1304        | 90.032239        | -20.152614       | 27.12±0.30 | 29.16±0.84 | 26.16±0.10 | 24.81±0.06 | 24.75±0.09 | 24.82±0.09 | 24.85±0.06 | 6.1 <sup>+0.2</sup> <sub>-0.3</sub> | 6.1 <sup>+0.1</sup> <sub>-0.3</sub> |
| Abell2163-1163         | 243.944229       | -6.146962        | > 27.7     | 29.21±1.23 | 26.54±0.15 | 24.87±0.06 | 24.69±0.09 | 24.64±0.07 | 24.86±0.06 | 6.2 <sup>+0.3</sup> <sub>-0.2</sub> | 6.2 <sup>+0.2</sup> <sub>-0.2</sub> |
| Abell2163-1612         | 243.918938       | -6.155229        | 28.03±0.89 | 28.70±0.86 | 25.96±0.08 | 24.90±0.07 | 24.84±0.10 | 24.88±0.09 | 24.94±0.06 | 6.0 <sup>+0.3</sup> <sub>-0.4</sub> | 6.0 <sup>+0.1</sup> <sub>-0.4</sub> |
| PLCKG287+32-3078       | 177.708907       | -28.097272       | > 27.9     | 27.39±0.40 | 27.44±0.40 | 25.41±0.13 | 24.90±0.14 | 25.16±0.15 | 24.96±0.08 | 1.4 <sup>+6.2</sup> <sub>-0.2</sub> | 6.5 <sup>+0.9</sup> <sub>-0.5</sub> |
| Abells295-0250         | 41.374456        | -53.030668       | 28.13±0.69 | > 28.8     | 27.05±0.20 | 25.10±0.07 | 24.93±0.11 | 25.09±0.11 | 25.04±0.07 | 6.3 <sup>+0.3</sup> <sub>-0.2</sub> | 6.3 <sup>+0.3</sup> <sub>-0.2</sub> |
| RXS0603+42-S-5318      | 90.835657        | 42.156162        | ...        | 28.06±0.47 | 26.87±0.12 | 25.47±0.09 | 25.04±0.10 | 25.30±0.11 | 25.12±0.06 | 1.4 <sup>+5.0</sup> <sub>-0.2</sub> | 6.0 <sup>+0.1</sup> <sub>-4.9</sub> |
| RXC2211-03-0547        | 332.929227       | -3.827773        | > 28.1     | > 28.7     | 25.50±0.08 | 25.20±0.09 | 25.09±0.14 | 25.18±0.13 | 25.20±0.09 | 5.7 <sup>+0.2</sup> <sub>-0.5</sub> | 5.5 <sup>+0.1</sup> <sub>-0.6</sub> |

**Notes:** The full tables of the  $z=6$  sample, including all ancillary HST data, will be made available in the online journal version. The brightest (in H160) 40 candidates are shown here as an example of the format. All magnitudes are given as observed (lensed) isophotal AB magnitudes.

<sup>a</sup> The online tables will use the full cluster name and ID as used by the released RELICS photometric catalogs.

<sup>b</sup> The EAZY photometric redshifts assuming a flat prior in magnitude, along with their 2- $\sigma$  uncertainty. Cases where the uncertainty reaches  $\Delta z > 2$  are due to a secondary peak in probability at lower redshift.

<sup>c</sup> The BPZ photometric redshifts assuming a small prior in magnitude, along with their 2- $\sigma$  uncertainty. Throughout this work, the redshift we assume for each candidate is the average of the BPZ and EAZY estimates unless they differ by  $\Delta z > 1$  in which case we adopt the higher redshift solution.

**Table 3**  
 $z \sim 7$  Galaxy Candidates Behind 41 RELICS Clusters

| Object ID         | $\alpha_{J2000}$ | $\delta_{J2000}$ | $B_{435}$  | $V_{606}$  | $I_{814}$  | $Y_{105}$  | $J_{125}$  | $JH_{140}$ | $H_{160}$  | $z_{EZ}$                            | $z_{BPZ}$                           |
|-------------------|------------------|------------------|------------|------------|------------|------------|------------|------------|------------|-------------------------------------|-------------------------------------|
| RXC0600-20-0178   | 90.027105        | -20.120249       | 30.24±1.99 | 27.99±0.33 | 27.55±0.29 | 25.01±0.06 | 24.67±0.08 | 24.55±0.06 | 24.42±0.04 | 6.5 <sup>+0.3</sup> <sub>-0.4</sub> | 6.7 <sup>+0.5</sup> <sub>-0.1</sub> |
| MS1008-12-0326    | 152.630990       | -12.653099       | > 28.1     | 28.40±0.70 | . . .      | 25.26±0.09 | 24.83±0.10 | 24.68±0.07 | 24.55±0.05 | 7.2 <sup>+0.7</sup> <sub>-0.6</sub> | 7.2 <sup>+0.3</sup> <sub>-0.3</sub> |
| PLCKG287+32-0698  | 177.704968       | -28.070710       | 28.95±1.21 | > 28.5     | 28.59±0.78 | 25.11±0.08 | 24.95±0.12 | 24.98±0.10 | 25.00±0.07 | 6.9 <sup>+0.7</sup> <sub>-0.3</sub> | 6.7 <sup>+0.5</sup> <sub>-0.3</sub> |
| PLCKG287+32-0777  | 177.719902       | -28.071524       | 28.73±1.00 | 28.47±0.64 | > 28.7     | 25.38±0.09 | 25.04±0.11 | 25.09±0.10 | 25.16±0.07 | 7.5 <sup>+0.2</sup> <sub>-0.7</sub> | 7.2 <sup>+0.2</sup> <sub>-0.6</sub> |
| PLCKG287+32-2235  | 177.716360       | -28.087833       | > 28.1     | 28.84±0.90 | > 28.6     | 25.33±0.09 | 25.14±0.13 | 25.18±0.12 | 25.17±0.07 | 7.3 <sup>+0.3</sup> <sub>-0.5</sub> | 7.0 <sup>+0.3</sup> <sub>-0.5</sub> |
| Abell3192-1076    | 59.711133        | -29.946217       | 29.05±0.70 | 32.74±3.39 | 29.90±1.17 | 25.59±0.09 | 25.34±0.14 | 25.40±0.12 | 25.32±0.08 | 7.1 <sup>+0.6</sup> <sub>-0.4</sub> | 6.8 <sup>+0.5</sup> <sub>-0.2</sub> |
| Abell1300-0226    | 172.983602       | -19.915016       | 27.77±0.39 | 30.15±1.28 | 29.06±0.90 | 25.97±0.11 | 25.58±0.13 | 25.92±0.15 | 25.62±0.08 | 7.3 <sup>+0.4</sup> <sub>-1.0</sub> | 6.7 <sup>+0.7</sup> <sub>-0.4</sub> |
| RXC0911+17-0419   | 137.787292       | 17.781433        | . . .      | . . .      | 28.87±0.50 | 25.36±0.09 | 25.65±0.18 | 25.25±0.11 | 25.64±0.10 | 6.9 <sup>+0.3</sup> <sub>-0.2</sub> | 6.7 <sup>+0.2</sup> <sub>-0.1</sub> |
| Abell1300-0534    | 172.985370       | -19.924202       | 27.81±0.42 | > 29.2     | 28.97±0.89 | 26.00±0.12 | 25.84±0.18 | 25.82±0.15 | 25.94±0.11 | 6.8 <sup>+0.2</sup> <sub>-0.5</sub> | 6.6 <sup>+0.6</sup> <sub>-0.4</sub> |
| Abell3192-0033    | 59.719401        | -29.911883       | > 29.4     | 29.09±0.50 | 28.84±0.48 | 26.07±0.11 | 26.44±0.28 | 26.05±0.17 | 26.07±0.12 | 6.8 <sup>+0.4</sup> <sub>-0.5</sub> | 6.6 <sup>+0.4</sup> <sub>-0.3</sub> |
| PLCKG287+32-0792  | 177.700898       | -28.071636       | > 28.8     | 29.47±0.91 | > 29.2     | 26.79±0.19 | 26.71±0.30 | 26.37±0.19 | 26.24±0.11 | 7.3 <sup>+0.6</sup> <sub>-1.1</sub> | 1.6 <sup>+6.2</sup> <sub>-0.3</sub> |
| ACT0102-49-2551   | 15.725680        | -49.232616       | 29.16±0.86 | 28.97±0.56 | 29.66±1.18 | 25.98±0.10 | 25.79±0.15 | 25.92±0.14 | 26.25±0.12 | 7.0 <sup>+0.3</sup> <sub>-0.4</sub> | 6.7 <sup>+0.3</sup> <sub>-0.2</sub> |
| ACT0102-49-2391   | 15.723132        | -49.239372       | 27.90±0.37 | > 29.3     | > 28.8     | 26.39±0.15 | 25.99±0.19 | 26.29±0.21 | 26.26±0.14 | 7.0 <sup>+0.7</sup> <sub>-0.5</sub> | 6.7 <sup>+0.5</sup> <sub>-0.4</sub> |
| MS1008-12-0312    | 152.647497       | -12.652450       | > 28.8     | 29.15±0.76 | . . .      | 26.50±0.15 | 26.40±0.22 | 26.60±0.22 | 26.31±0.12 | 7.1 <sup>+0.2</sup> <sub>-2.2</sub> | 6.8 <sup>+0.5</sup> <sub>-5.5</sub> |
| PLCKG287+32-2252  | 177.703898       | -28.084229       | > 28.7     | > 29.2     | 28.57±0.46 | 26.73±0.18 | 26.85±0.32 | 26.90±0.28 | 26.40±0.13 | 6.5 <sup>+0.7</sup> <sub>-4.7</sub> | 1.2 <sup>+4.8</sup> <sub>-0.4</sub> |
| MS1008-12-0313    | 152.647304       | -12.652520       | 28.13±0.49 | > 29.1     | . . .      | 26.49±0.16 | 26.52±0.26 | 26.37±0.19 | 26.46±0.14 | 6.8 <sup>+0.7</sup> <sub>-0.7</sub> | 6.4 <sup>+0.6</sup> <sub>-5.3</sub> |
| Abell1763-1500    | 203.831009       | 40.988866        | > 28.9     | 30.76±1.66 | 29.18±0.85 | 26.55±0.14 | 26.84±0.13 | 26.35±0.22 | 26.50±0.09 | 6.7 <sup>+0.6</sup> <sub>-1.0</sub> | 6.4 <sup>+0.5</sup> <sub>-5.0</sub> |
| SPT0254-58-0476   | 43.593763        | -58.949693       | > 29.1     | 28.78±0.42 | 28.82±0.56 | 26.52±0.15 | 26.84±0.33 | 26.49±0.21 | 26.50±0.14 | 6.7 <sup>+0.6</sup> <sub>-5.2</sub> | 6.4 <sup>+0.6</sup> <sub>-5.2</sub> |
| RXC0032+18-0571   | 8.052543         | 18.131884        | 28.81±0.88 | 31.32±2.32 | 28.74±0.67 | 26.48±0.16 | 26.42±0.26 | 26.82±0.29 | 26.50±0.16 | 6.7 <sup>+0.7</sup> <sub>-1.5</sub> | 6.4 <sup>+0.8</sup> <sub>-0.8</sub> |
| SMACS0723-73-1317 | 110.785854       | -73.467361       | 28.78±0.71 | > 29.6     | > 29.2     | 26.24±0.14 | 26.43±0.23 | 26.56±0.23 | 26.53±0.15 | 7.0 <sup>+0.5</sup> <sub>-0.4</sub> | 6.7 <sup>+0.4</sup> <sub>-0.4</sub> |
| Abell520-1342     | 73.531755        | 2.903624         | 28.88±0.70 | 28.88±0.56 | > 29.2     | 26.86±0.20 | 26.53±0.26 | 26.36±0.19 | 26.61±0.16 | 7.6 <sup>+0.4</sup> <sub>-1.1</sub> | 6.9 <sup>+0.3</sup> <sub>-5.9</sub> |
| CL0152-13-0410    | 28.182402        | -13.946921       | > 28.9     | . . .      | . . .      | 26.46±0.15 | 26.87±0.14 | 26.58±0.24 | 26.66±0.12 | 6.7 <sup>+0.2</sup> <sub>-0.4</sub> | 6.4 <sup>+0.2</sup> <sub>-0.3</sub> |
| RXC0142+44-1088   | 25.714213        | 44.623339        | 30.41±1.54 | > 29.7     | > 29.4     | 27.23±0.22 | 27.00±0.28 | 27.30±0.30 | 26.68±0.13 | 7.0 <sup>+1.0</sup> <sub>-1.9</sub> | 1.3 <sup>+6.2</sup> <sub>-0.3</sub> |
| PLCKG287+32-2457  | 177.706999       | -28.090180       | 28.81±0.78 | > 28.9     | 29.68±1.17 | 27.15±0.24 | 27.46±0.54 | 27.63±0.48 | 26.69±0.17 | 6.7 <sup>+1.0</sup> <sub>-5.6</sub> | 1.4 <sup>+0.7</sup> <sub>-5.7</sub> |
| CL0152-13-0259    | 28.182517        | -13.971709       | > 28.8     | . . .      | . . .      | 26.40±0.16 | 26.38±0.10 | 26.36±0.23 | 26.70±0.14 | 7.0 <sup>+0.5</sup> <sub>-0.5</sub> | 6.7 <sup>+0.4</sup> <sub>-0.4</sub> |
| MS1008-12-0227    | 152.648835       | -12.649399       | > 28.9     | > 29.1     | . . .      | 27.10±0.24 | 27.59±0.55 | 26.74±0.24 | 26.72±0.17 | 7.2 <sup>+0.7</sup> <sub>-2.9</sub> | 1.3 <sup>+6.1</sup> <sub>-0.4</sub> |
| PLCKG004-19-2704  | 289.272136       | -33.544955       | > 28.7     | 29.28±0.83 | > 28.9     | 26.91±0.20 | 26.68±0.28 | 27.13±0.32 | 26.72±0.17 | 7.0 <sup>+0.9</sup> <sub>-0.7</sub> | 6.7 <sup>+0.7</sup> <sub>-5.6</sub> |
| PLCKG004-19-1983  | 289.261526       | -33.530310       | 28.28±0.51 | > 29.4     | 28.87±0.65 | 26.55±0.14 | 26.71±0.26 | 26.72±0.22 | 26.75±0.15 | 6.7 <sup>+0.6</sup> <sub>-0.7</sub> | 6.4 <sup>+0.5</sup> <sub>-0.5</sub> |
| Abell2163-1715    | 243.931878       | -6.162199        | > 28.3     | 30.59±1.85 | > 29.2     | 26.90±0.21 | 26.78±0.30 | 26.97±0.29 | 26.77±0.17 | 7.0 <sup>+0.8</sup> <sub>-1.5</sub> | 6.7 <sup>+0.7</sup> <sub>-0.8</sub> |
| SMACS0723-73-0599 | 110.840288       | -73.449995       | > 28.5     | > 29.2     | 29.64±1.22 | 27.17±0.23 | 27.30±0.42 | 26.77±0.23 | 26.82±0.16 | 6.5 <sup>+1.3</sup> <sub>-5.6</sub> | 1.3 <sup>+6.2</sup> <sub>-0.4</sub> |
| PLCKG287+32-0221  | 177.714041       | -28.064780       | > 28.7     | > 29.1     | 29.49±1.00 | 26.75±0.28 | 26.72±0.50 | 26.79±0.40 | 26.85±0.31 | 6.8 <sup>+1.2</sup> <sub>-5.3</sub> | 6.4 <sup>+1.0</sup> <sub>-0.6</sub> |
| MACS0257-23-0787  | 44.303042        | -23.441137       | > 29.3     | . . .      | > 30.1     | 27.49±0.27 | 27.05±0.32 | 27.31±0.33 | 26.94±0.17 | 7.5 <sup>+0.9</sup> <sub>-1.2</sub> | 6.9 <sup>+0.9</sup> <sub>-5.5</sub> |
| SPT0615-57-0548   | 93.973142        | -57.777418       | 28.72±0.60 | > 29.7     | 29.70±0.58 | 27.09±0.20 | 26.94±0.29 | 26.70±0.21 | 26.95±0.17 | 6.6 <sup>+1.2</sup> <sub>-0.8</sub> | 6.6 <sup>+0.8</sup> <sub>-0.4</sub> |
| PLCKG287+32-1887  | 177.691357       | -28.083799       | 27.78±0.36 | > 29.3     | > 29.3     | 27.42±0.30 | 27.26±0.42 | 27.98±0.62 | 27.00±0.20 | 7.0 <sup>+1.4</sup> <sub>-5.7</sub> | 1.3 <sup>+6.0</sup> <sub>-0.4</sub> |
| PLCKG004-19-1156  | 289.272414       | -33.520949       | 30.16±1.62 | 30.32±1.41 | > 29.0     | 27.21±0.25 | 26.93±0.31 | 27.05±0.29 | 27.01±0.20 | 7.4 <sup>+0.7</sup> <sub>-5.8</sub> | 6.7 <sup>+0.9</sup> <sub>-5.6</sub> |
| MACS0553-33-0463  | 88.335048        | -33.703438       | > 29.8     | 29.65±0.67 | 29.78±0.71 | 27.36±0.25 | 27.34±0.39 | 27.32±0.32 | 27.15±0.19 | 6.6 <sup>+1.2</sup> <sub>-5.7</sub> | 6.5 <sup>+0.9</sup> <sub>-5.4</sub> |
| MACS0553-33-0865  | 88.327049        | -33.713029       | > 29.8     | 29.05±0.43 | 30.30±0.98 | 26.96±0.19 | 27.10±0.33 | 27.54±0.39 | 27.16±0.20 | 6.8 <sup>+0.7</sup> <sub>-0.7</sub> | 6.6 <sup>+0.6</sup> <sub>-0.6</sub> |
| Abell1763-1564    | 203.830702       | 40.987242        | > 29.0     | 31.92±2.48 | > 29.2     | 27.05±0.19 | 27.01±0.13 | 27.16±0.37 | 27.18±0.13 | 7.1 <sup>+0.7</sup> <sub>-0.7</sub> | 6.6 <sup>+0.7</sup> <sub>-0.6</sub> |
| Abell1763-0817    | 203.807526       | 41.002688        | > 29.2     | 29.57±0.68 | 31.39±2.26 | 27.49±0.25 | 26.99±0.11 | 27.15±0.35 | 27.19±0.12 | 7.7 <sup>+0.6</sup> <sub>-2.4</sub> | 7.2 <sup>+0.6</sup> <sub>-1.3</sub> |
| PLCKG287+32-2199  | 177.717592       | -28.087374       | > 29.1     | 29.23±0.62 | > 29.6     | 27.24±0.21 | 27.84±0.54 | 27.55±0.38 | 27.21±0.19 | 6.9 <sup>+0.8</sup> <sub>-5.4</sub> | 2.5 <sup>+1.1</sup> <sub>-1.6</sub> |
| Abell3192-0728    | 59.734516        | -29.933640       | > 30.1     | > 30.2     | 32.49±2.54 | 27.16±0.18 | 27.15±0.30 | 27.93±0.47 | 27.27±0.19 | 7.0 <sup>+0.7</sup> <sub>-0.5</sub> | 6.7 <sup>+0.6</sup> <sub>-0.4</sub> |

**Notes:** The full table of the  $z=7$  sample, including all ancillary HST data, will be made available in the online journal version. The brightest (in H160) 40 candidates are shown here as an example of the format. All magnitudes are given as observed (lensed) isophotal AB magnitudes.

**Table 4**  
 $z \sim 8$  Galaxy Candidates Behind 41 RELICS Clusters

| Object ID        | $\alpha_{J2000}$ | $\delta_{J2000}$ | $B_{435}$        | $V_{606}$        | $I_{814}$        | $Y_{105}$        | $J_{125}$        | $JH_{140}$       | $H_{160}$        | $z_{EZ}$            | $z_{BPZ}$           |
|------------------|------------------|------------------|------------------|------------------|------------------|------------------|------------------|------------------|------------------|---------------------|---------------------|
| PLCKG287+32-2013 | 177.687797       | -28.076086       | $28.13 \pm 0.78$ | $> 28.5$         | $29.87 \pm 1.64$ | $25.61 \pm 0.19$ | $24.97 \pm 0.19$ | $24.84 \pm 0.13$ | $24.88 \pm 0.09$ | $7.6^{+0.7}_{-1.3}$ | $7.5^{+0.3}_{-0.8}$ |
| Abell1763-1434   | 203.833374       | 40.990179        | $> 28.6$         | $> 29.1$         | $> 28.8$         | $27.70 \pm 0.43$ | $26.40 \pm 0.10$ | $26.13 \pm 0.22$ | $26.17 \pm 0.08$ | $8.4^{+1.2}_{-1.8}$ | $8.2^{+0.4}_{-6.9}$ |
| Abells295-0568   | 41.401024        | -53.040518       | $> 28.9$         | $> 29.5$         | $31.78 \pm 2.48$ | $27.07 \pm 0.22$ | $26.02 \pm 0.17$ | $26.38 \pm 0.19$ | $26.35 \pm 0.12$ | $8.1^{+0.3}_{-1.7}$ | $7.7^{+0.4}_{-0.9}$ |
| RXC0911+17-0143  | 137.793971       | 17.789752        | . . .            | . . .            | $31.41 \pm 1.85$ | $27.18 \pm 0.24$ | $26.12 \pm 0.17$ | $26.61 \pm 0.21$ | $26.45 \pm 0.13$ | $8.1^{+0.3}_{-1.6}$ | $7.7^{+0.4}_{-0.9}$ |
| PLCKG287+32-2032 | 177.722594       | -28.085070       | $28.33 \pm 0.55$ | $28.00 \pm 0.31$ | $> 29.2$         | $27.81 \pm 0.41$ | $26.59 \pm 0.26$ | $26.87 \pm 0.28$ | $26.74 \pm 0.17$ | $8.2^{+0.5}_{-6.8}$ | $1.6^{+6.0}_{-0.5}$ |
| MACS0553-33-0219 | 88.354035        | -33.697948       | $30.36 \pm 0.98$ | $> 30.0$         | $29.78 \pm 0.63$ | $28.11 \pm 0.41$ | $26.75 \pm 0.23$ | $26.85 \pm 0.21$ | $27.19 \pm 0.18$ | $8.3^{+0.5}_{-6.9}$ | $7.9^{+0.4}_{-6.6}$ |
| SPT0615-57-1048  | 93.969721        | -57.789586       | $> 29.6$         | $33.58 \pm 3.51$ | $30.97 \pm 1.30$ | $28.15 \pm 0.36$ | $27.36 \pm 0.31$ | $28.06 \pm 0.46$ | $27.73 \pm 0.24$ | $7.7^{+0.7}_{-6.7}$ | $6.7^{+1.3}_{-5.5}$ |
| Abell1763-0460   | 203.824976       | 41.009117        | $28.74 \pm 0.46$ | $> 30.0$         | $29.50 \pm 0.74$ | $29.94 \pm 1.16$ | $27.58 \pm 0.15$ | $27.26 \pm 0.29$ | $27.78 \pm 0.16$ | $8.5^{+1.2}_{-7.1}$ | $8.1^{+0.4}_{-7.2}$ |

**Notes:** The full table of the  $z=8$  sample, including all ancillary HST data, will be made available in the online journal version. All eight candidates are shown here as an example of the format. All magnitudes are given as observed (lensed) isophotal AB magnitudes.